© Copyright 2017

Jiangang Han

Seismic Study of Tremor, Deep Long-Period Earthquakes, and Basin Amplification of Ground Motion

Jiangang Han

A dissertation

submitted in partial fulfillment of the

requirements for the degree of

Doctor of Philosophy

University of Washington

2017

Reading Committee:

John Vidale, Chair

Ken Creager

Heidi Houston

Program Authorized to Offer Degree:

Earth and Space Sciences

University of Washington

Abstract

Seismic Study of Tremor, Deep Long-Period Earthquakes, and Basin Amplification of Ground Motion

Jiangang Han

Chair of the Supervisory Committee:
Professor John Vidale
Earth and Space Sciences

In this thesis, we use seismic data and seismological tools to investigate three topics, (1) triggering between slow slip (tremor as proxy) and nearby small earthquakes, (2) mechanisms of deep-long period earthquakes beneath Mount St. Helens, and (3) ground motion amplification in Seattle Basin. In Chapter 1, we investigate 12-year earthquake and tremor catalogs for southwest Japan, and find nearby small intraslab earthquakes are weakly correlated with tremor. In particular, intraslab earthquakes tend to be followed by tremor more often than expected at random, while the excess number of tremor before earthquakes is not as significant. The underlying triggering mechanism of tremor and inferred slow slip by earthquakes is most likely to be the dynamic stress changes (several to several tens of kPa) rather than the much smaller static stress changes. In Chapter 2, we use the catalog DLPs as templates to search for repeating

events at Mount St. Helens (MSH). We have detected 277 DLPs, compared to only 22 events previously in the catalog from 2007 to 2016. Three templates from the catalog are single events, while all other templates produced matches, identifying loci of repeated activity. Overall, the detected DLPs show no significant correlation with either the subduction zone tremor and slow slip (ETS) west of MSH, or the shallow seismicity. Temporal analysis shows an elevated rate of DLPs at time of compressional tidal stress, suggesting their possible association with magmatic and/or fluid activity. We observed variable S wave polarization of the DLPs from the most productive DLP source region, indicating their source mechanisms are not identical. In Chapter 3, we use noise correlation to retrieve the empirical green's functions (EGFs) in Seattle Basin. Consistent amplitudes measured from noise EGFs, teleseismic S wave and numerical simulations all suggest the usefulness of the amplitude of EGFs. For surface wave with period of 5-10 sec propagating from west to east, the ground motion is amplified by a factor of up to 3 within the basin. The bias of EGFs from noise heterogeneity and uncertainties of synthetics due to inaccuracy of velocity model are still to be investigated.

TABLE OF CONTENTS

LIST OF FIGURES

LIST OF TABLES

ACKNOWLEDGEMENTS

I am indebted to many great people who gave me a lot of help and support during my study at University of Washington. Firstly, I owe a lot to my advisor John Vidale, who I feel so lucky to have had in my graduate study and whole life. John has been providing great research advices with his insightful perspectives, with his understanding of techniques, and particularly with his kindness. I also thank John for his understanding and kind support on my career pursuit.

Also, I would like to thank the others in my PhD committee, professor Heidi Houston, Ken Creager, David Schmidt, and William Wilcock for their help and kindness. My thanks goes to Heidi, for her encouragement and advices on my research, for the great courses she taught, continuum mechanics and theoretical seismology, for her significant input in the first two Chapters of my thesis. To Ken, for his great courses, the solid earth, theoretical seismology, and inverse theory, for his help on technical issues and great suggestions on Chapter 2 and other questions and discussions in general. To David, for his geodesy courses, for his help in processing the GPS data, and for his valuable contributions to Chapter 2. To William, who is my Graduate School Representative (GSR) in my committee, for his valuable questions and comments in my general and final examinations.

In addition, I would like to thank professor Kazushige Obara and Dr. Kevin Chao, for providing the seismic data used in Chapter 1, and for their contributions in interpreting and discussing the results

My thanks also goes to the seismology and PNSN people at UW, thank you all for being such a great group. Thanks to Paul Bodin for his help in allocating my financial support and providing computing resources for my research. To Carl Ulberg, Shelly Chestler, Kelley Hall, Mark Welch, Mika Thompson, Ian Stone, Erin Wirth, Xiaofeng Meng, Alicia Hotovek, Justin Sweet, Kate

Allstadt, for their help and making such a great study group. To the faculties, students, and staffs in the department of Earth and Space Sciences, for making such a great environment for sharing and learning. Thanks to all the members from the iMUSH team, for their effort in field work and acquiring high quality data, which is partially used in Chapter 2 of this thesis.

Thanks to my roommates at Seattle, Y. G., Y. H. O., S. C. Z., Y. A. M., Y. Z., and T. C. S., for the happy time we spent together.

Finally, I would like to thank my family for their long-time love and supports in my study and life. To my parents and little brother, who may not ever understand my study and research, but thank you, for your endless love and sacrifices for our family. Finally, to my beloved Dou, for your persistent love and encouragement, which always makes me full of passion and hope for career and life.

CHAPTER 0. THESIS STRUCTURE

Seismic data and seismological tools have been widely used to study the structure of the earth, earthquakes, and earthquake hazards. In this thesis, we use seismology as a tool to investigate three scientific questions, with each chapter for one topic. In the last chapter (Chapter 4), we take a summary by highlighting the most important results and conclusions for studies in all three chapters.

In the three following chapters, we examine seismic data and use various seismic methods to investigate scientific questions concerning subduction zone environments. The first one that we study in Chapter 1 is on the triggering relationship between subduction zone tremor and slab earthquakes. Previous studies have shown that tremor (and slow slip) can be modulated by various types of external driving forces, for example from solid earth and ocean tides, surface waves of large distant earthquakes, and static stress change associated with earthquakes. The question we attempt to answer in Chapter 1 is if the tremor (slow slip) at the subduction plate interface can be triggered by nearby slab earthquakes, or vice versa. Two typical and well-studied subduction zones for tremor study are the Cascadia subduction zone and the Nankai subduction zone in southwest Japan. To investigate the triggering between tremor and slab earthquakes, large earthquake and tremor catalogs with high resolution would be desired. We choose the Nankai subduction zone in which to conduct this research, because in the Cascadia subduction zone the number of slab earthquakes is not large enough for robust statistics. Both tremor and slab earthquakes are well documented at Nankai subduction zone. We analyzed the dataset, and present the results and discussions on our question.

Mount St. Helens volcano is an active volcano, belonging to the Cascadia volcanic chain. The magmatic activity beneath Mount St. Helens is associated with subduction and dehydration of Juan de Fuca slab to the west and below the active volcano. In Chapter 2, using seismic data and tools, we investigate the activity and physical mechanisms of deep-long period earthquakes (DLP) beneath Mount St. Helens volcano. This study could help us understand the dynamic processes in a volcanic system, and potentially could also be useful for volcanic eruption forecasting.

In Pacific Northwest, the Cascadia megathrust has ruptured every 300 to 600 hundred years, and the populous Puget Sound region are exposed to this seismic risk. In addition to the megathrust, deep-focus earthquakes and shallow crustal earthquakes could also be destructive events. Seattle sits on top of a thick sedimentary basin, which increases the hazard by trapping and amplifying propagating waves. One central component in evaluating and mitigating the earthquake hazard is to better quantify the ground motion amplifications in this region. In chapter 3, we looked at this question by using noise correlation to provide independent constraints on amplification of the ground motion in the basin. Results from other datasets and methods are also presented in this chapter for comparison, cross validation, and understating the uncertainties.

CHAPTER 1. TRIGGERING OF TREMOR AND INFERRED SLOW SLIP BY SMALL EARTHQUAKES AT THE NANKAI SUBDUCTION ZONE IN SOUTHWEST JAPAN

1.1 INTRODUCTION

Slow slip, occurring at the brittle-ductile transition zone with long duration of days to months, constitutes a third mode, in addition to stick-slip (earthquakes) and continuous aseismic slip, of strain release at plate boundaries. Geodetically-observed slow slip events have been reported in various subduction zones (e.g., Dragert et al., 2001; Obara et al., 2004) as well as on the strike-slip San Andreas fault (Linde et al., 1996). Some slow slip events are accompanied by emergent seismic signals of long duration known as tremor (Obara, 2002; Rogers and Dragert, 2003) and low frequency earthquakes (LFEs) (Obara, 2002; Katsumata and Kamaya, 2003; Shelly et al., 2006, 2007). These slip phenomena are often called episodic tremor and slip (ETS). Both nonvolcanic tremor and slow slip have been observed in Southwest Japan, where the Philippine plate subducts beneath the Eurasian plate. There have been a tremendous number of tremor (over twenty thousand used in this study) and slow slip events detected in this region. As has been reported in the Cascadia subduction zone (Rogers and Dragert, 2003), the tremor and slow slip in the Nankai subduction zone are found to be highly correlated in space and time (Obara et al., 2004; Obara and Hirose, 2006).

The strong spatiotemporal coincidence of these slip phenomena suggests the same underlying physical mechanism, which is different from that of regular stick-slip earthquakes. The spatial and temporal correlation between regular earthquakes and slow slip (or tremor) is of great importance to understand the slip behavior at the fault plane. Also, study of the possible triggering of regular earthquakes from the neighboring tremor may help to mitigate the earthquake hazards

by monitoring tremor activity and slow slip at the Nankai subduction zone as well as other places in the world.

Tectonic tremor, occurring near the brittle-ductile transition zone of the fault, is sensitive to stress changes from tidal loading (Rubinstein et al., 2008; Nakata et al., 2008; Houston, 2014) and from dynamic shaking of propagating surface waves from distant large earthquakes (Miyazawa and Mori, 2006; Rubinstein et al., 2007; Chao et al., 2012, 2013). On the other hand, slow slip has been observed to coincide with triggered seismicity, for instance, at Hawaii (Segall et al., 2006), at New Zealand subduction zone (Delahaye et al., 2009) and at Boso Peninsula, central Japan (Hirose et al., 2014). Spatiotemporal correlation of five small earthquakes around an ETS event has been reported at the Cascadia subduction zone (Vidale et al., 2011). These correlations suggest the potential for significant triggering between slow slip and earthquakes (Kato et al., 2012), and thus the potential to forecast big earthquakes by monitoring slow slip and tremor activity. Studies of triggering between slow slip (or tremor) and earthquakes have been mostly based on an individual big earthquake or slow slip event; the small dataset limits the generality of the implications. Our direct comparison between tremor rate and local small earthquake seismicity from a large dataset (about twenty thousands events in each catalog) over a longer period (eleven and a half years) sheds more light on the as yet poorly-resolved triggering relation between slow slip, as revealed by tremor, and regular earthquakes.

In this study, we investigate the relation between the earthquake seismicity and the activity of tremor at Nankai subduction zone in Japan by looking into the spatial-temporal correlation between small intraslab earthquakes and tremor in this region. The shallow earthquakes in the overlying upper crust are 20 km or further away from the tremor, and the stress loading from these events would be minor. So we focus our work on the nearby intraslab earthquakes that would be

more likely to trigger or to be triggered by tremor. We find there is higher probability that tremors follow bigger earthquakes. The excess probability for earthquakes following tremor is not as significant, although there are marginally more than background. The triggering stress for the observed triggered tremor is most likely to be dynamic shaking of propagating wave rather than static stress associated with the earthquakes.

1.2 DATA AND METHOD

We examine two data catalogs. One is the tremor catalog (Obara et al., 2010) with time resolution of one hour. The other is the earthquake catalog from the Japan Meteorological Agency (JMA). The JMA catalog clearly separates the earthquakes and LFEs (Katsumata and Kamaya, 2003), and we only use the intraslab earthquakes below the plate interface which is 7 km above the oceanic Moho estimated by Shiomi et al. (2006). To investigate the correlation between the tremor and intraslab earthquakes in this region, we use data from January 2001 to June 2012.

Table 1.1. Earthquake numbers and averaged magnitude for each magnitude bins.

Magnitude	Event number	Averaged magnitude
M=[0.7 0.9]	7924	0.7879
M=[1.0 1.7]	8754	1. 2647
M=[1.8 2.6]	2509	2. 0988
M>=2.7	768	3. 1924

The hourly tremor catalog (Obara et al., 2010) that we use is constructed with the assumption of depth fixed at the plate interface, which is assumed to be 5 km above the oceanic Moho depth estimated by Shiomi et al. (2006). In this study we use this original tremor catalog, but assume 7-km oceanic crust thickness. This shifts the tremor 2 km shallower, which causes little horizontal

shift in the tremor location, due to the insensitivity of travel time to depth in event location. Examining crustal thicknesses of 5 km and 6 km, in addition to 7 km, we determined that crustal thickness does not significantly influence our results.

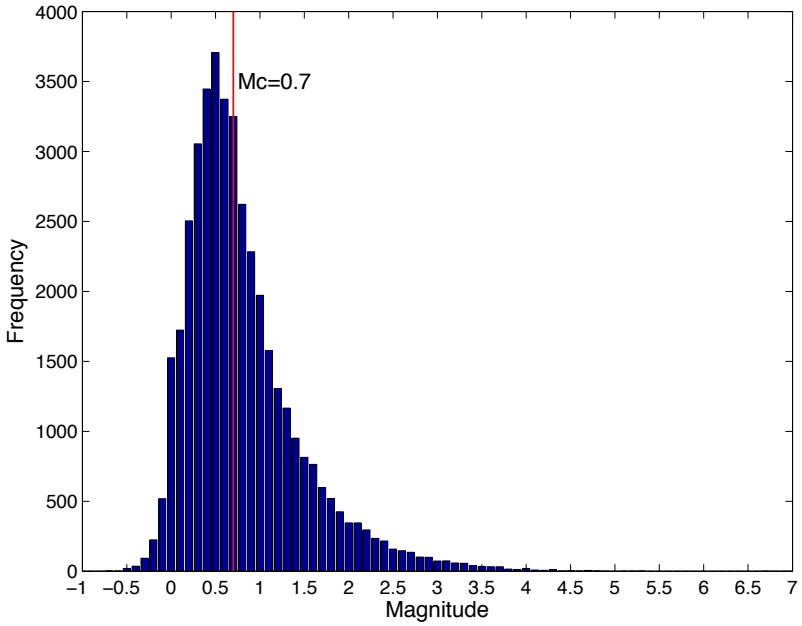

Figure 1.1. Intraslab earthquake magnitude histogram. We choose M=0.7 as magnitude of completeness.

We restrict our catalog to only include those intraslab earthquakes within 20 km horizontal distance of any tremor, so these are the events analyzed below. Given the weak effect that we find, events at greater distances are not expected to show correlations, and are not in this initial reconnaissance. The earthquakes investigated in this study have magnitude $M_j = 0.7$ or greater (JMA magnitude, which is approximately equal to moment magnitude for $M_j < 4.5$, Katsumata, 1996), which is the estimated completeness magnitude (Figure 1.1). We take JMA earthquake magnitude as equal to moment magnitude when evaluating stress level later in the paper. We

decluster the earthquake catalog following Reasenberg (1985) so that we can minimize the degradation of the final correlation result by aftershocks and earthquake swarms. The final intraslab earthquake catalog that we used in this correlation study contains 19,955 events (Table 1.1), with 4.2% of original events removed by declustering.

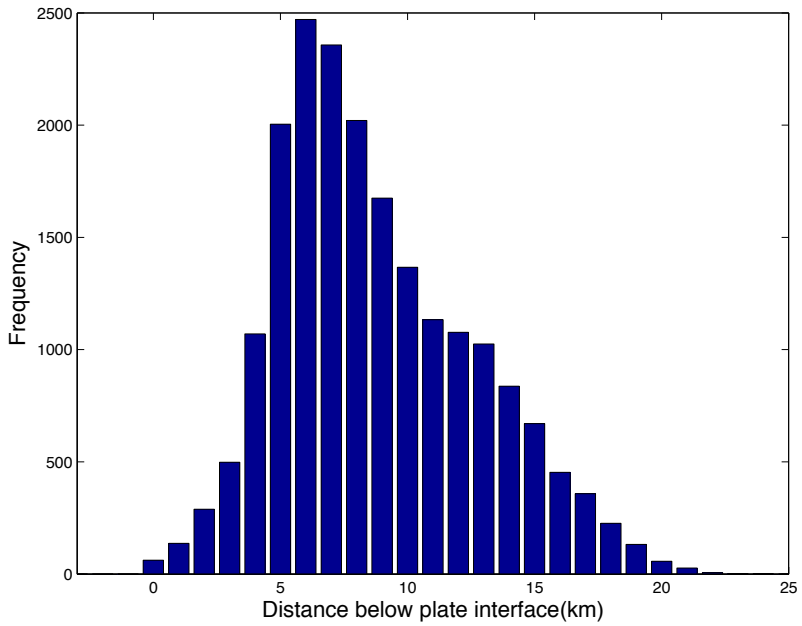

Figure 1.2. Histogram of intraslab earthquakes distance below plate interface. The total number of intraslab earthquakes we used in this study is 19955.

To evaluate the degree of triggering between earthquakes and tremor, we first find how many earthquakes and tremor are spatially and temporally close to each other. For each earthquake (T_e, $\mathbf{X}_e$), we search the tremor catalog and keep all those tremor (T_t, $\mathbf{X}_t$) that satisfy the following conditions:

$$\mathrm{Dmin} < |\mathbf{X}_t - \mathbf{X}_e| \leq \mathrm{Dmax},\ \ \mathrm{Tmin} < T_t - T_e < \mathrm{Tmax} \qquad (1.1)$$

$$\mathrm{Dmin} < |\mathbf{X}_e - \mathbf{X}_t| \leq \mathrm{Dmax},\ \ \mathrm{Tmin} < T_e - T_t < \mathrm{Tmax} \qquad (1.2)$$

in which T_e is the occurrence time of earthquake e and T_t is time of hourly episode of tremor t; $\mathbf{X}_e$, $\mathbf{X}_t$ are the three-dimensional locations of earthquake e and tremor t; Dmin and Dmax specify the proximity bins in space; Tmin and Tmax specify the proximity bins in time. The distance bins we used are 0-8, 8-11, 11-14, 14-17, 17-20 km, and time bins are 0-6, 6-12, 12-24, 24-48 hours. The criterion (1.1) and (1.2) above are for the evaluation of earthquakes triggering tremor and triggered by tremor, respectively.

We perform this evaluation process again using the same tremor catalog (T_t, $\mathbf{X}_t$) but a temporally-randomized earthquake catalog (T_e^*, $\mathbf{X}_e$), where T_e^* has a uniformly random distribution between the beginning and the end of the investigated time interval. We apply this algorithm 500 times and estimate the expectation and standard deviation of correlations for each spatial and temporal proximity. Tests with 1000 times did not appreciably change the results. Using the observed distribution of earthquakes in assessing correlation is necessary because earthquakes are far from uniformly distributed across the subduction zone.

Comparing the number of earthquakes that correlated with some tremor and the expected number of correlated earthquakes from a randomized catalog gives insight into the frequency of triggering between earthquakes and tremor. We use the ratio between observed correlated earthquake number and that expected at random to quantify the degree of triggering between tremor and earthquakes.

Table 1.2. Correlated earthquake numbers within 12 hours for each distance and magnitude bin.

Magitude\Distance	0-8 km	8-11 km	11-14 km	14-17 km	17-20 km
M=[0.7 0.9]	25	52	77	91	105
M=[1.0 1.7]	23	62	90	96	113
M=[1.8 2.6]	5	21	29	42	33
M=[2.7 6.7]	5	14	14	13	11

Table 1.3. Averaged magnitude of correlated earthquakes within 12 hours for several distance and magnitude bin.

Magnitude\Distance	0-8 km	8-11 km	11-14 km	14-17 km	17-20 km
M=[0.7 0.9]	0.7720	0.7885	0.7992	0.7912	0.8038
M=[1.0 1.7]	1.2348	1.2742	1.2756	1.3010	1.2805
M=[1.8 2.6]	2.0600	2.1810	2.1310	2.0786	2.1545
M=[2.7 6.7]	3.1600	3.3143	3.2214	3.2000	3.6636

1.3 Results and Discussion

Intraslab earthquakes occurred up to about 20 km below the plate interface, with a peak distribution around the oceanic Moho (Figure 1.2, Figure 1.3b, also see Shelly et al., 2006). To reiterate, since these intraslab earthquakes and tremor are sometimes very near to each other, we are searching for the component of seismicity in response to the slow slip or tremor activity, and also tremor response to earthquake activity. The small but significant correlations between the tremor and intraslab earthquakes that we find here shows there is triggering between the two.

For a range of distance and time delay parameters, we find the ratio is distinctly higher than one, especially for those earthquakes with magnitude bigger than 2 (Figure 1.4b and 1.8b). There are about two to six times more intraslab earthquakes with nearby tremor shortly after them than expected from randomized catalogs. This means earthquakes have triggered some tremor. We find higher ratios for earthquakes in higher magnitude ranges, showing that, as expected, bigger earthquakes are more likely to trigger tremor (Figure 1.4b and 1.8b, also see Figure 1.13). The biggest magnitude of a correlated earthquake is 4.7. Within each magnitude bin, there is a systematically decreasing ratio with increased distance (Figure 1.4b), which is physically expected from the lower stress loading of the more distant earthquakes (see Figure 1.14). Quantitative stress estimates based on distance and magnitude range are given and discussed later in the paper (Figure

1.15). Similarly, with increased delay time, we find the ratio starts high at short times, then with time decreases down to one, the expected value when there is little triggering. This suggests the triggering mechanism has a time scale less than about 24 hours (Figure 1.8b).

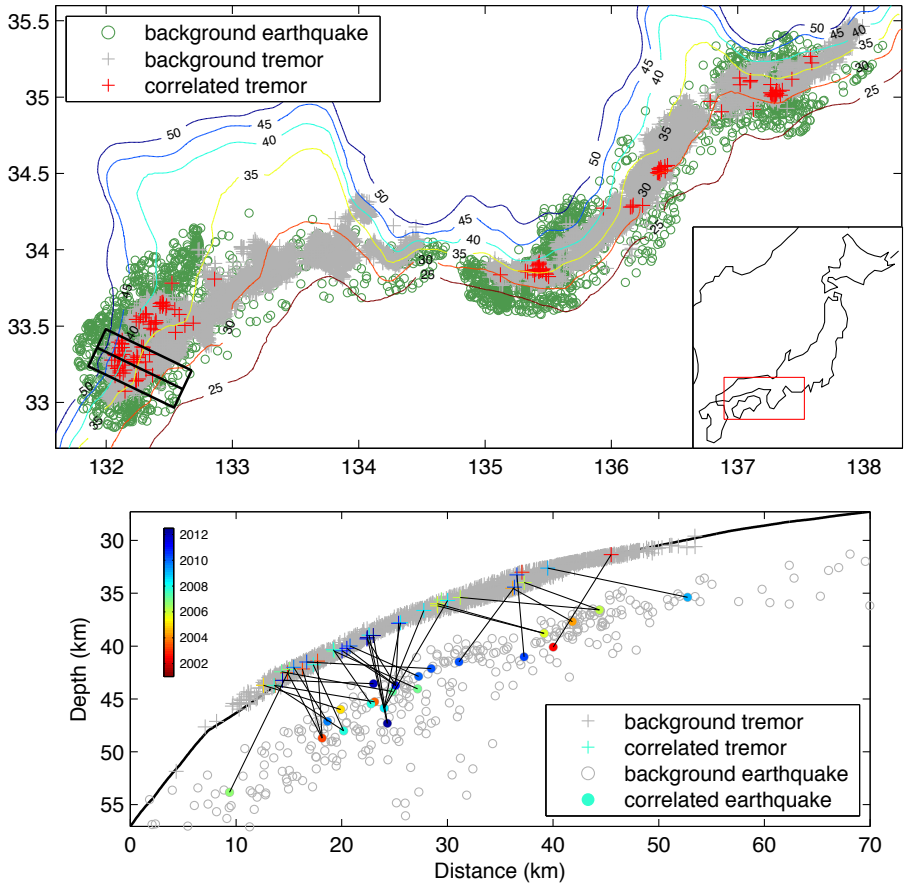

Figure 1.3. Tremor and intraslab earthquakes at Nankai subduction zone from January 2001 to June 2012. (a) Background intraslab earthquakes (green circles) with M≥2.5 are plotted. Correlated earthquakes and tremor (red pluses) are those within of 14 km and 12 hours. Colored contours indicate the plate interface depth in km; black box indicates the cross section position. (b) Cross section shows the correlation between tremor at the plate interface and the slab earthquakes (M≥1.8) below. Tremor and earthquakes of the same color and connected by a black line occurred close together in time.

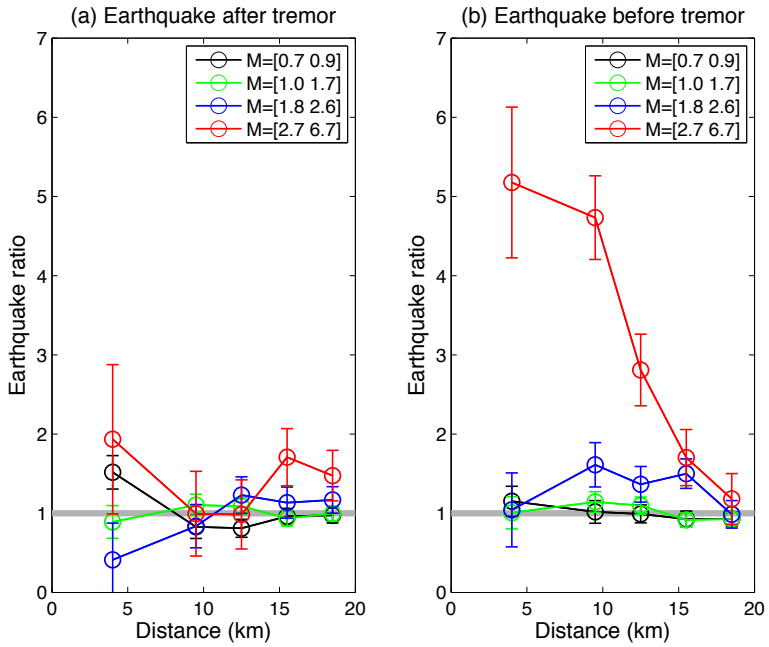

Figure 1.4. Earthquake ratio (correlated earthquakes in real catalog divided by correlated earthquakes in randomized catalog) versus distance. The distance bins are 0-8, 8-11, 11-14, 14-17, 17-20km. The time delay limit considered is 12 hours. (a) Earthquake ratio for earthquake after tremor. (b) Earthquake ratio for earthquake before tremor. The thick horizontal grey bar represents the level in the randomized catalog. Error bars are calculated by σ/N, where N is the average number of correlated earthquakes from randomized catalogs, and σ is its standard deviation. See table 1.2 and table 1.3 for correlated event numbers and average magnitude in each magnitude and distance bin. See Figures 5-7 for the results with other time interval.

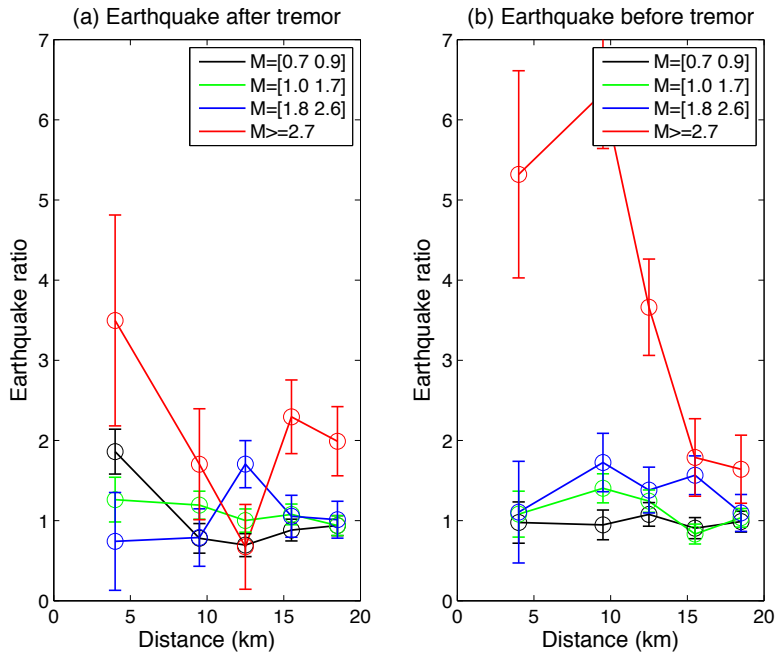

Figure 1.5. Same as Figure 1.4, but time is within 6 hours.

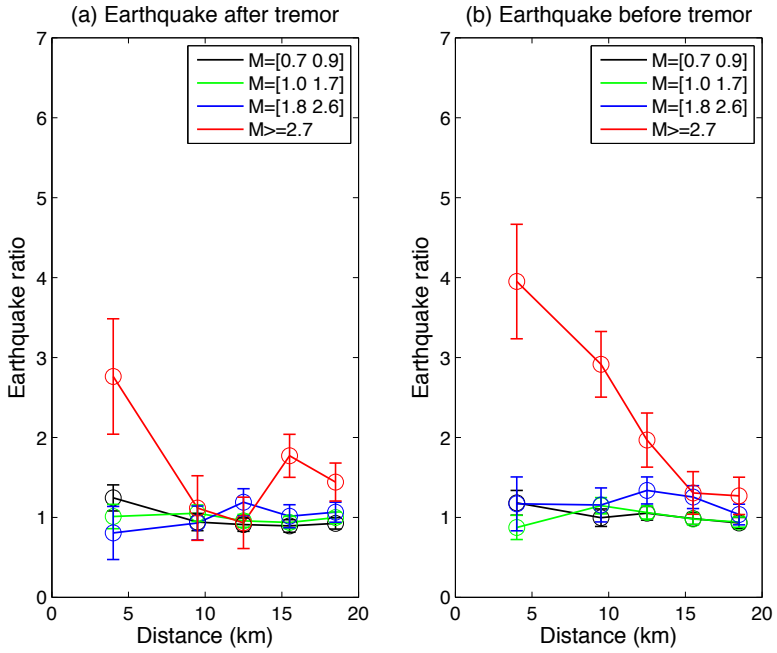

Figure 1.6. Same as Figure 1.4, but time is within 24 hours.

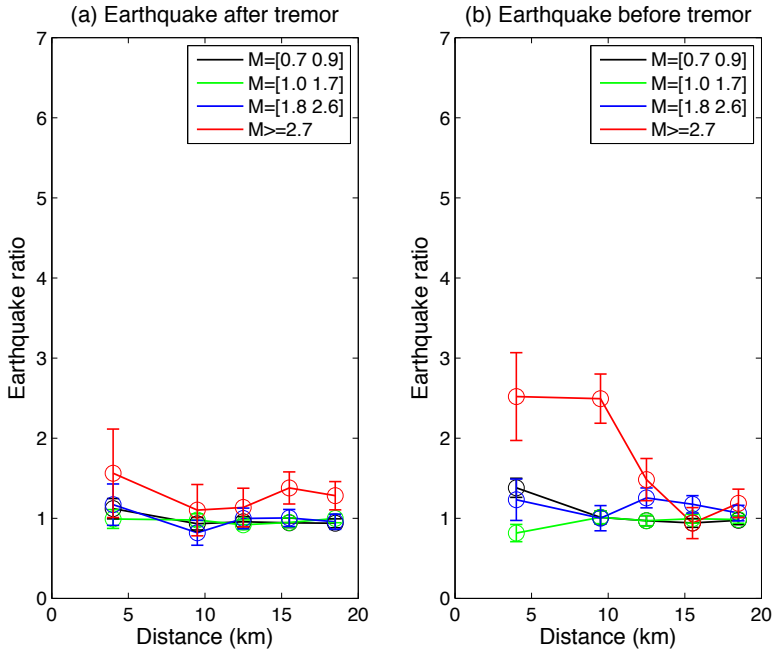

Figure 1.7. Same as Figure 1.4, but time is within 48 hours.

Whether the tremor (or more likely the slow slip driving it) triggers seismicity is also interesting and important for mitigation of earthquake hazard. In Southwest Japan the tremor occurred at the plate interface with depth variation from 30 km to 45 km (Figure 1.3), and it has been not very clear about how close tremor is from rupture zone of the shallow megathrust. The potential for the updip megathrust triggering by deep tremor has not been well understood yet. Intraslab earthquakes just beneath the plate interface at the tremor zone could be triggered by nearby tremor and slow slip, and these intraslab events, in turn, might as well contribute to the stress loading for the potential updip megathrust.

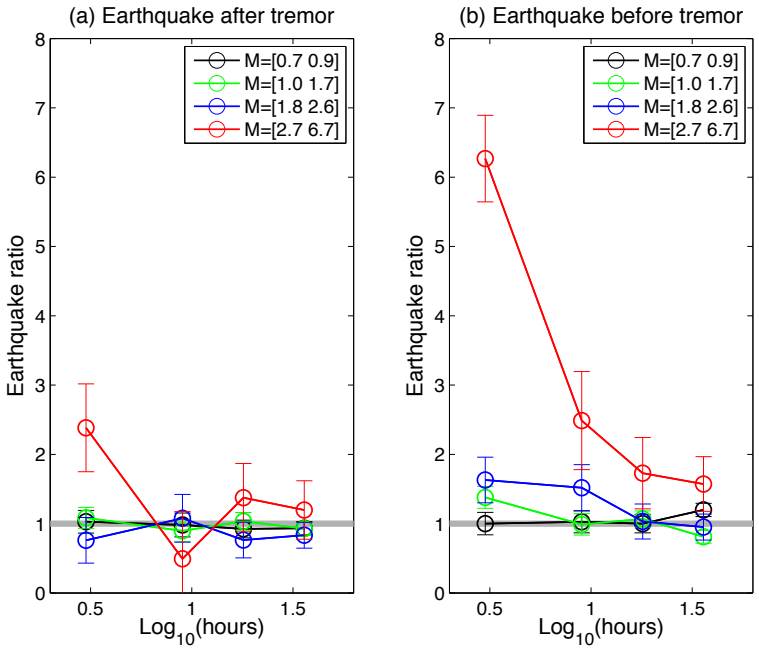

Figure 1.8. Earthquake ratio (same definition as in Figure 1.4) versus with time delay between earthquake and tremor. The time bins are 0-6, 6-12, 12-24 and 24-48 hours respectively. The distance range is within 11 km. (a) Earthquake ratio for earthquake after tremor. (b) Earthquake ratio for earthquake before tremor. The thick horizontal grey bar represents the level in the randomized catalog. Error bars defined as in Figure 1.4. See supplementary Figures 1.9-1.12 for the results with other distance range.

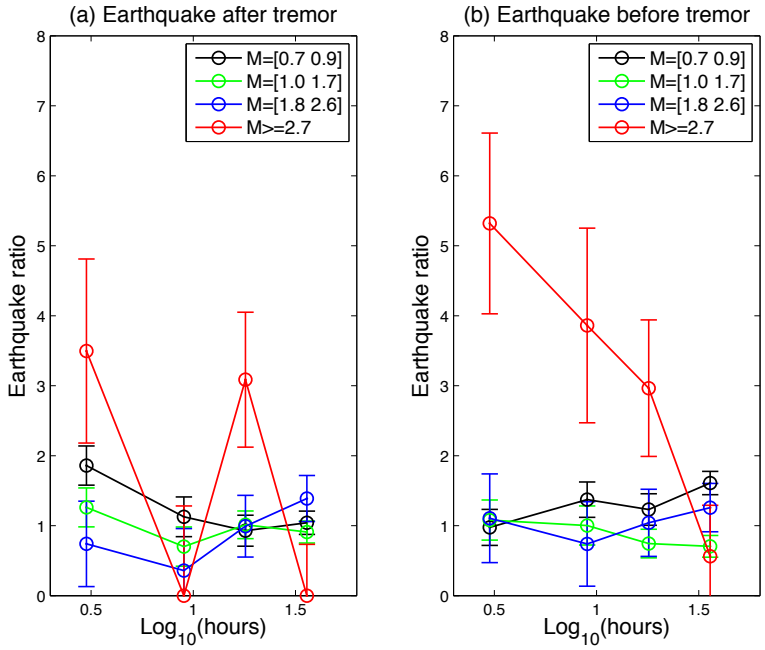

Figure 1.9. Same as Figure 1.8, but distance is within 8 km.

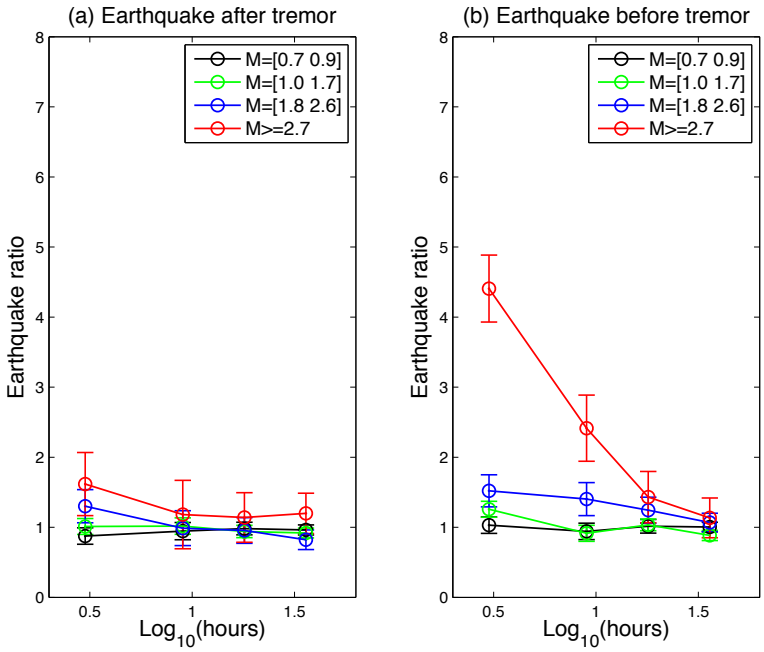

Figure 1.10. Same as Figure 1.8, but distance is within 14 km.

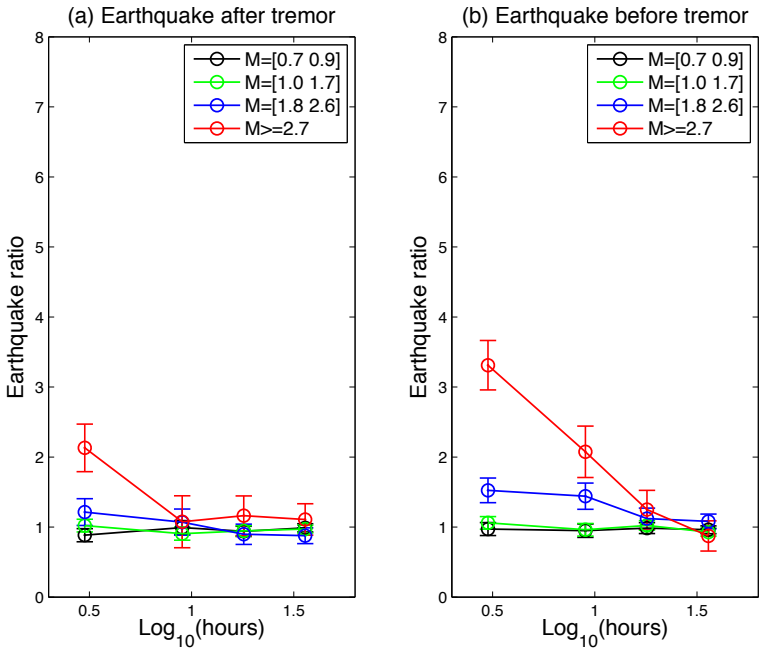

Figure 1.11. Same as Figure 1.8, but distance is within 17 km.

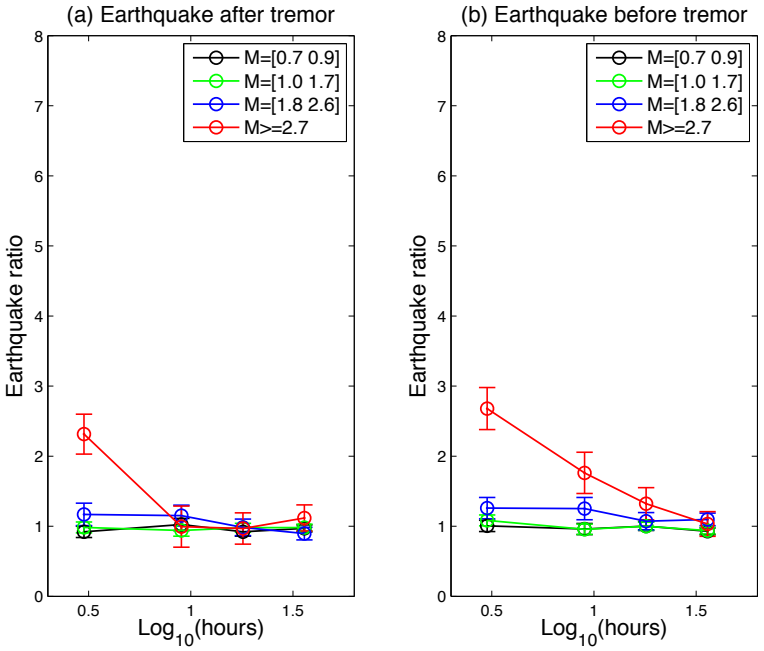

Figure 1.12. Same as Figure 1.8, but distance is within 20 km.

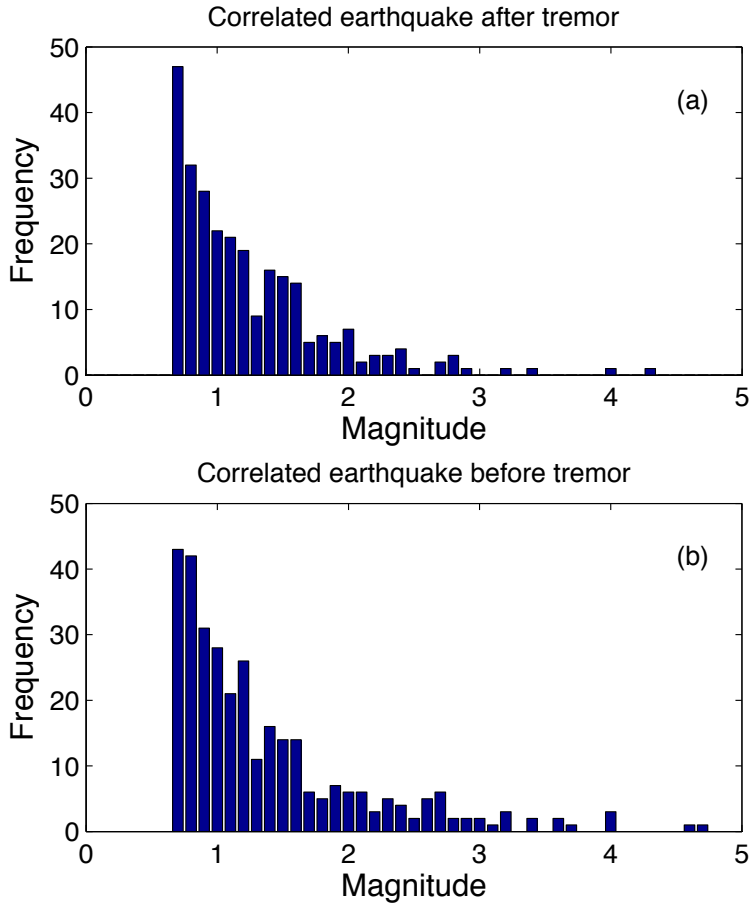

Figure 1.13. Correlated earthquake magnitude histogram. (a) correlated earthquake after tremor, (b) correlated earthquake before tremor.

We find the triggering of earthquakes by tremor is not as significant as the triggering of tremor by earthquakes (Figure 1.4a and 1.8a). The ratio of apparently-correlated events between the real catalog and randomized catalogs also shows a decreasing pattern with the delayed time, albeit much weaker. Although this trend could indicate triggering of earthquakes by tremor events, the correlated earthquake number is within the standard deviation of the expectation derived in the randomized searches. That is to say the resultant ratio, in spite of being larger than one, is not a compelling indicator of tremor triggering earthquakes. This result is not unexpected, given that

the stress changes associated with tremor at the plate interface may well be too small to trigger intraslab earthquakes. The ratio higher than one might be from the contributions of a few earthquakes within a period of extensive slow slip, as was shown for Cascadia subduction zone by Vidale et al. (2011), which claims an elevated rate of tiny intraslab earthquakes in response to an ETS event. Previous studies have also found increased seismicity rate accompanying slow slip event at Hawaii (Segall et al., 2006), New Zealand (Delahaye et al., 2009), and Boso Peninsula, central Japan (Hirose et al., 2014), probably due to stress loading from the slow slip. Similarly, we think the triggering of intraslab earthquakes by tremor at Nankai subduction zone, although very weak, is likely due to the stress changes associated with slow slip events.

The different triggering potential between earthquakes and tremor is probably because both the dynamic and static stress changes associated with earthquakes are larger than those associated with tremor. Moreover, tremor is thought to occur at the plate interface with low effective stress, and thus is very sensitive to driving stresses. Stress change due to tidal loading, with magnitude of a few kPa or less, is enough to modulate tremor activity (Shelly et al., 2007; Rubinstein et al., 2008; Houston, 2014) and slow slip (Hawthorne and Rubin, 2010) by a factor of two to three. Previous studies have also observed many tremor events amplified or triggered by dynamic shaking from distant large earthquakes (Rubinstein et al., 2007; Peng et al., 2008; Chao et al., 2012, 2013), with amplitudes of a few tens of kPa. Thus, stress of amplitude around 1 kPa seems necessary in order to measurably trigger tremor.

Possible tremor triggering mechanisms include static Coulomb stress change and dynamic stress changes caused by shaking that result from the earthquake seismic wave passage. These two mechanisms might both contribute to the observed correlations. To understand the triggering mechanism of tremor at Nankai subduction zone, we evaluated both the static stress and dynamic

stress associated with earthquakes at the tremor location. First, we calculate the static stress tensor at the location of tremor resulting from a double-couple point source using a code based on Okada (1992). The maximum static shear stress generated at the tremor location was on the order of several to 10's of Pa, which is too small to trigger tremor, as it is far smaller than the tidal stresses that only moderately influence tremor (Nakata et al., 2008). We conclude that the triggering of tremor by static stress change of the intraslab earthquakes, at least for the dataset that we studied, is negligible.

Then, we calculated the dynamic stress tensor at the time of the S wave from a double-couple point source in a wholespace. A wholespace is an adequate assumption here because the distances between earthquakes and tremor and the wavelengths of the transient S waves are small relative to the depth. The strain tensor was calculated from the spatial gradient of the far-field S-wave displacement vector, and is dominated by a term with the time derivative of the source pulse and 1/r falloff with distance. Thus, the duration of the transient S wave affects the amplitude of the strain. Triangular source time functions were estimated from the Madariaga (1976) model with stress drop of 3 MPa (Shearer, 2009). The duration ranges from 0.005 to 0.1 s for the earthquake magnitude range studied here. The stress tensor was determined from the strain tensor using Hooke's law, assuming a Poisson solid with density of 3200 kg/m^3, and shear-wave velocity of 4400 m/s, which equates to a rigidity of 6.2×10^{10} Pa.

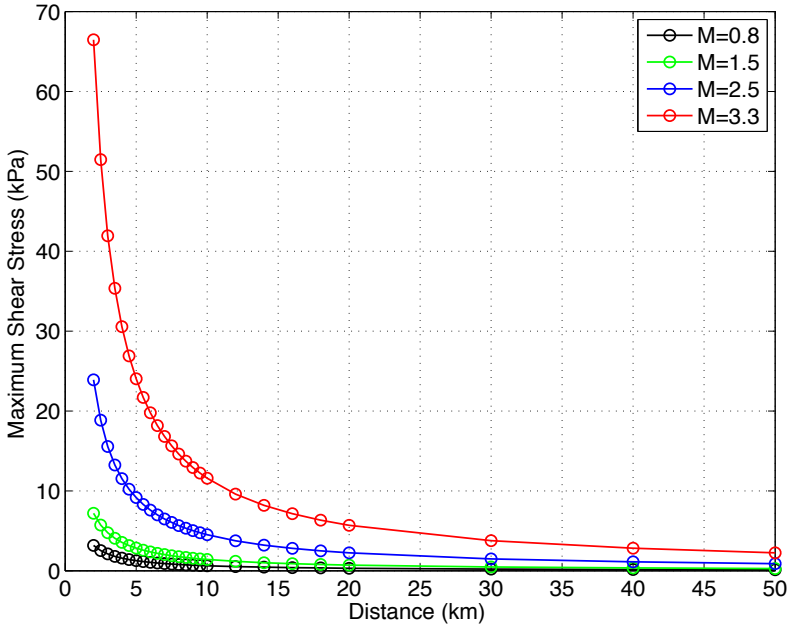

Figure 1.14. Maximum shear stresses of S-wave decrease as a function of distance.

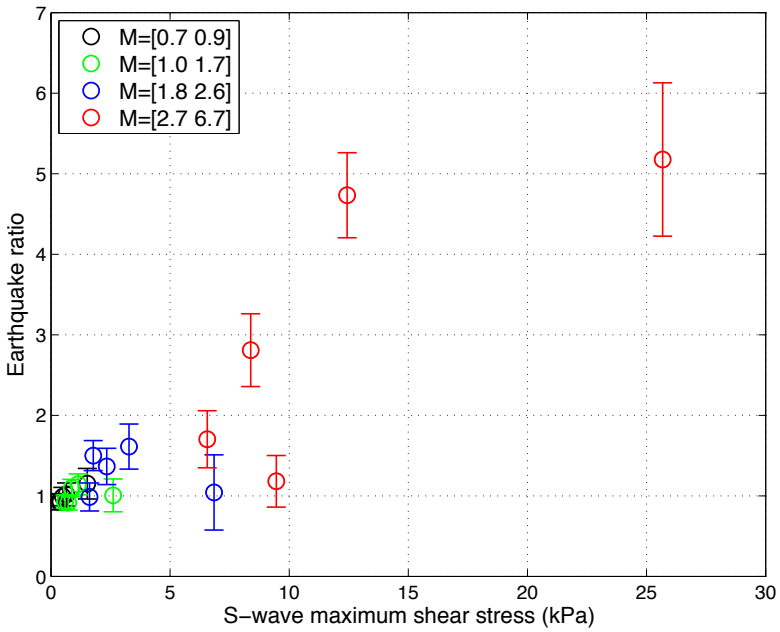

Figure 1.15. Earthquake ratio (defined as in Figure 1.4) variation with maximum shear stress calculated for S-wave from the earthquakes. For the stress calculation, the distances are binned as in Figure 1.4 and magnitude is averaged among the correlated earthquakes in each bin.

We focus on shear, rather than Coulomb stress, for simplicity and because friction on the plate interface appears to be low (e.g., Houston 2014). Maximum shear stresses from the dynamic S-wave stress tensor are half the difference between the maximum and minimum principal stress. The dynamic shear stresses are 2 to 3 orders of magnitude higher than the static stresses at the distances and magnitudes of the triggering quakes. Rather than guess focal mechanisms and trust precise relative locations, we simply plot the amplitude averaged across the focal sphere (Boore and Boatwright, 1984). Figure 1.14 shows shear stresses versus distance for earthquakes of different magnitudes. Shear stresses of a few to 10's of kPa are generated for the largest average magnitude value as shown by red circles in Figure 1.15. These are on the order of the minimum tremor triggering stresses from surface waves of large distant earthquakes (e.g., 2-3 kPa by Rubinstein et al., 2009 and Peng et al., 2009, 7-8 kPa by Chao et al., 2012, and 10 kPa by Chao et al., 2013) and an order of magnitude greater than the tidal stresses that trigger tremor and slow slip on the Cascadia and Japan subduction zones (e.g., Rubinstein et al., 2008; Nakata et al., 2008; Hawthorne and Rubin, 2010; Houston, 2014). Figure 1.15 shows that the triggering ratio depends systematically on the applied shear stress for the distance and magnitude ranges studied here. Large shear stresses, due to either very close distance or large earthquake moment release or both, are a plausible cause of the tremor triggered at the plate interface.

Tremor triggering by regional earthquakes has been studied in central California (Guilhem et al., 2010), where four regional earthquakes with magnitude 6.6, 6.9, 7.2, 7.2 were observed to trigger tremor. The inferred threshold of triggering stress by these regional events is 1 kPa, the same magnitude as for teleseismic events. Our results suggest that even a very brief stress increase can increase tremor rate by 2 to 7 times over background rates. The stress levels that trigger tremor

are the same magnitude or only slightly higher than those for other much more prolonged stressing processes that trigger tremor; surface waves of distant large earthquakes and Earth and ocean tides. The durations of stressing for the points in Figure 1.15 also vary by more than an order of magnitude, but given the similarity of triggering thresholds between these tiny events and tidal stresses lasting hours, duration doesn't affect thresholds as strongly as amplitude. From figure 1.15, we estimate the stress magnitude for tremor rate increasing due to the nearby intraslab earthquakes to be ~10 kPa. The stress range we evaluated here with notable tremor rate increase is also comparable with the static stress level that accounts for increased tremor rate (Nadeau and Guilhem, 2009). Thus, it seems that a change of over several kPa of either static or dynamic stress might increase the tremor rate by a measurable level, suggesting a very weak fault for tremor genesis.

1.4 Conclusions

By investigating decade-long catalogs of earthquakes and tremor at Nankai subduction zone in Japan, we find that small intraslab earthquakes trigger tremor with the effectiveness of such triggering dependent on magnitude. The triggering of earthquakes by tremor is not as significant. This difference in triggering between tremor and earthquakes is probably due to the different stress change magnitudes associated with the two categories of events. Dynamic shear stress of incoming S-waves from the nearby earthquakes is several or several tens of kilopascals, and is observed to increase the tremor rate by a factor of two to six, comparable to triggering observed from much longer period surface waves and tides of similar stress amplitude.

1.5 REFERENCES

Boore, D.M. and J.Boatwright (1984). Average body-wave radiation coefficients, Bull. Seism. Soc. Am. 74, 1615–1621.

Chao, K., Z. Peng, C. Wu, C.-C. Tang, and C.-H. Lin (2012). Remote triggering of non-volcanic tremor around Taiwan, Geophys. J. Int. 188, no. 1, 301–324, doi: 10.1111/j.1365-246X.2011.05261.x.

Chao, K., Z. Peng, H. Gonzalez-Huizar, C. Aiken, B. Enescu, H. Kao, A. A. Velasco, K. Obara, and T. Matsuzawa (2013), A global search for triggered tremor following the 2011 Mw9.0 Tohoku earthquake, Bull. Seism. Soc. Am., 103(2b), doi:10.1785/0120120171.

Delahaye, E. J., J. Townend, M. E. Reyners, and G. Rogers (2009), Microseismicity but no tremor accompanying slow slip in the Hikurangi subduction zone, New Zealand, Earth Planet. Sci. Lett., 277 (1–2), 21–28.

Douglas, A., J. Beavan, L. Wallace, and J. Townend (2005), Slow slip on the northern Hikurangi subduction interface, New Zealand, Geophys. Res. Lett., 32 (16), doi:10.1029/2005GL023607.

Dragert, H., K.Wang, and T. S. James (2001), A Silent Slip Event on the Deeper Cascadia Subduction Interface, Science, 292 (5521), 1525–1528.

Guilhem, A., Peng, Z.&Nadeau, R.M., 2010. High-frequency identification of non-volcanic tremor triggered by regional earthquakes, Geophys. Res. Lett, 37, L16309, doi:10.1029/2010GL044660.

Hawthorne, J. C., and A. M. Rubin (2010), Tidal modulation of slow slip in Cascadia, J. Geophys. Res., 115, B09406, doi:10.1029/2010JB007502.

Hirose, H., T. Matsuzawa, T. Kimura, and H. Kimura (2014), The Boso slow slip events in 2007 and 2011 as a driving process for the accompanying earthquake swarm, Geophys. Res. Lett., 41, 2778–2785, doi:10.1002/2014GL059791.

Houston H., Response of tremor and slow slip to tidal stress: Constraints on fault friction and weakening, Nature GeoScience, submittted, 2014

Katsumata, A. (1996), Comparison of magnitudes estimated by the Japan Meteorological Agency with moment magnitudes for intermediate and deep earthquakes, Bull. Seismol. Soc. Am., 86, 832–842.

Kato, A., Obara, K., Igarashi, T., Tsuruoka, H., Nakagawa, S., Hirata, N., 2012. Propagation of slow slip leading up to the 2011 Mw 9.0 Tohoku-Oki Earthquake. Science 335, 705–708.

Katsumata, A., and N. Kamaya, Low-frequency continuous tremor around the Moho discontinuity away from volcanoes in the southwest Japan, Geophys. Res. Lett. , 30(1), 1020, doi:10.1029/2002GL0159812, 2003.

Linde, A. T., M. T. Gladwin, M. J. S. Johnston, R. L. Gwyther, and R. G. Bilham (1996), A slow earthquake sequence on the San Andreas fault, Nature, 383, 65–68.

Madariaga, R. (1976). Dynamics of an expanding circular fault, Bull. Seismol. Soc. Am. , 66 , 639–666.

Miyazawa, M., and J. Mori (2006), Evidence suggesting fluid flow beneath Japan due to periodic seismic triggering from the 2004 Sumatra-Andaman earthquake, Geophys. Res. Lett., 33, L05303, doi:10.1029/2005GL025087.

Nadeau, R. M. & Guilhem, A. Nonvolcanic tremor evolution and the San Simeon and Parkfield, California, earthquakes. Science 325, 191–193 (2009).

Nakata, R., N. Suda, and H. Tsuruoka (2008), Nonvolcanic tremor resulting from the combined

effect of Earth tides and slow slip events, Nat. Geosci.,1, 676–678, doi:10.1038/ngeo288.

Obara, K. (2002), Nonvolcanic deep tremor associated with subduction in southwest Japan, Science, 296, 1679–1681, doi:10.1126/science.1070378.

Obara, K., H. Hirose, F. Yamamizu, and K. Kasahara (2004), Episodic slow slip events accompanied by non-volcanic tremors in southwest Japan subduction zone, Geophys. Res. Lett., 31, doi:10.1029/2004GL020848.

Obara, K., and H. Hirose (2006), Non-volcanic deep lowfrequency tremors accompanying slow slips in the southwest Japan subduction zone, Tectonophysics, 417, 33–51.

Obara, K., Tanaka, S., Maeda, T. & Matsuzawa, T. Depth-dependent activity of non-volcanic tremor in southwest Japan. Geophys. Res. Lett. 37, L13306 (2010).

Okada, Y. (1992), Internal deformation due to shear and tensile faults in a half-space, Bull. Seism. Soc. Am., 82, 1018–1040.

Peng, Z., J.E. Vidale, K.C. Creager, J.L. Rubinstein, J. Gomberg, and P. Bodin (2008), Strong tremor near Parkfield, CA excited by the 2002 Denali Fault earthquake, Geophys. Res. Lett., 35, L23305, doi:10.1029/2008GL036080.

Peng, Z., J. E. Vidale, A. G. Wech, R. M. Nadeau, and K. C. Creager (2009), Remote triggering of tremor along the San Andreas Fault in central California, Journal of Geophysical Research, 114(B00A06), doi:10.1029/2008JB006049.

Reasenberg, P. (1985). Second-order moment of central California seismicity, 1969–1982, J. Geophys. Res. 90, 5479–5496.

Rogers, G., and H. Dragert (2003), Episodic Tremor and Slip on the Cascadia Subduction Zone: The Chatter of Silent Slip, Science, 300(5627), 1942-1943.

Rubinstein, J.L., J.E. Vidale, J. Gomberg, P. Bodin, K.C. Creager and S.D. Malone (2007), Non-volcanic tremor driven by large transient shear stresses, Nature, 448, doi:10.1038/nature06017, 579–582.

Rubinstein, J.L., M. La Rocca, J.E. Vidale, K.C. Creager, and A.G.Wech (2008), Tidal modulation of non-volcanic tremor, Science, 319, 186–189.

Rubinstein, J. L., J. Gomberg, J. E. Vidale, A. G. Wech, H. Kao, K. C. Creager, and G. Rogers (2009), Seismic wave triggering of nonvolcanic tremor, episodic tremor and slip, and earthquakes on Vancouver Island, J. Geophys. Res., 114, B00A01, doi:10.1029/2008JB005875.

Shearer, P.M. (2009). Introduction to Seismology. 2nd edn. New York: Cambridge University Press.

Shelly, D. R., G. C. Beroza, S. Ide, and S. Nakamula (2006), Low-frequency earthquakes in Shikoku, Japan, and their relationship to episodic tremor and slip, Nature, 442(7099), 188–191, doi:10.1038/nature04931.

Shelly, D. R., Beroza, G. C. & Ide, S. (2007a), Non-volcanic tremor and low frequency earthquake swarms. Nature, 446,305–307.

Shelly, D.R., G.C. Beroza, and S. Ide (2007b), Complex evolution of transient slip derived from precise tremor locations in western Shikoku, Japan. Geochem. Geophys. Geosyst., 8, Q10014, doi:10.1029/2007GC001640.

Shiomi, K., Obara, K., Sato, H., 2006. Moho depth variation beneath southwestern Japan revealed from the velocity structure based on receiver function inversion. Tectonophysics 420, 205–221.

Segall, P., E. K. Desmarais, D. Shelly, A. Miklius, and P. Cervelli (2006), Earthquakes triggered by silent slip events on Kilauea volcano, Hawaii, Nature, 442, 71–74.

Vidale, J. E., A. J. Hotovec, A. Ghosh, K. C. Creager, and J. Gomberg (2011), Tiny intraplate earthquakes triggered by nearby episodic tremor and slip in Cascadia, Geochem. Geophys. Geosyst., 12, Q06005, doi:10.1029/2011GC003559.

CHAPTER 2. DEEP LONG-PERIOD EARTHQUAKES (DLPS) BENEATH MOUNT ST. HELENS MODULATED BY TIDAL STRESS

2.1 INTRODUCTION

Deep long-period earthquakes (DLPs) have been observed in many volcanic settings, including the Cascade volcanoes (Nicholas et al., 2011), Aleutian arc volcanoes (Power et al., 2004), Japan (Aso et al., 2011; Aso and Ide, 2013), Hawaii (Aki and Koyanagi, 1981; Matoza et al., 2014) and many other places (e.g., Hill et al., 2002). These long-period events are characterized by (1) a lack of high-frequency energy as compared with regular earthquakes, (2) a long duration of coda waves, (3) infrequent occurrence, (4) a depth location below the crustal seismogenic zone. For example, DLPs at Mount St. Helens (MSH) extend to a depth of 42 km (Vidale et al., 2014).

Understanding the physical mechanism of DLPs could provide insights on (1) the magma/fluid migration process (e.g., Shapiro et al., 2017); (2) forearc mantle wedge dynamics (Vidale et al., 2014); (3) and volcanic eruption forecasting (e.g., Chouet et al., 1996). Based on observations, several hypotheses have been proposed to interpret the source process of DLPs, including dehydration embrittlement of already-serpentinized mantle material (e.g., forearc DLPs in western Oregon by Vidale et al., 2014), magma and/or fluid movement (e.g., Ukawa and Ohtake, 1987; Shapiro et al., 2017), thermal strain from magma cooling (Aso and Tsai, 2014), as well as others (e.g., Aki and Koyanagi, 1981; Chouet, 1996).

So far, neither a comprehensive understanding nor a compelling physical model for DLPs at MSH have been well-established, due to both the lack of high-quality data and limited investigation. In this study, we use almost ten years of seismic data from PNSN stations and the iMUSH (imaging Magma Under St. Helens) broadband array to study the DLPs beneath MSH. We first perform earthquake detection by taking DLPs in the PNSN catalog as templates for cross-

correlation matching. Then we analyze the correlations of DLPs with ETS, shallow seismicity, and solid Earth tides, and examine their focal mechanisms by polarization analysis of particle motions.

Table 2.1. DLPs cataloged by PNSN during the period 2007 to 2016.

Magnitude	Time (UTC)	Latitude	Longitude	Depth (km)
0.4	2016/09/14 08:14:02	46.1587	-122.1547	22.8
0.2	2016/09/14 08:13:28	46.1863	-122.1382	24.7
0.4	2016/07/03 09:32:41	46.1407	-122.0880	23.8
0.5	2016/04/24 08:54:50	46.1552	-122.1433	25.4
0.2	2015/03/18 17:39:23	46.1590	-122.1460	21.8
0.4	2015/03/18 17:39:14	46.1527	-122.1275	23.3
0.5	2014/10/04 16:26:35	46.1550	-122.1140	25.8
0.7	2014/10/04 16:21:51	46.1643	-122.1178	24.0
0.5	2014/07/29 15:18:04	46.1520	-122.1072	23.7
0.8	2014/07/23 15:30:12	46.1570	-122.0658	36.9
0.1	2014/07/11 06:07:21	46.1477	-122.1865	31.7
0.5	2014/07/11 06:06:25	46.1568	-122.0930	27.1
0.5	2014/06/29 13:50:27	46.1667	-122.0930	22.7
0.6	2014/04/17 12:23:10	46.1692	-122.1057	21.5
0.4	2012/10/08 23:09:32	46.1443	-122.1368	22.6
0.9	2011/10/19 02:07:12	46.1838	-122.1342	23.6
0.3	2010/08/24 00:54:44	46.1643	-122.0787	24.8
1.3	2009/04/29 22:47:11	46.1530	-122.0898	27.0
0.4	2009/04/19 22:11:31	46.1472	-122.1443	28.7
0.6	2007/12/17 21:07:09	46.1662	-122.1005	24.2
0.8	2007/08/16 16:11:07	46.3182	-122.3218	42.5
0.5	2007/05/22 03:41:45	46.2828	-122.2602	41.6

Time formatted as year/month/day hour:minute:second

Table 2.2. Stations and channels used in DLP detection.

Network	Station	Channel	Latitude	Longitude
CC	JRO	BHE	46.2751	-122.218
CC	JRO	BHN	46.2751	-122.218
CC	JRO	BHZ	46.2751	-122.218
CC	STD	BHE	46.2376	-122.224
CC	STD	BHN	46.2376	-122.224
CC	STD	BHZ	46.2376	-122.224
UW	YACT	BHE	45.9325	-122.419
UW	YACT	BHN	45.9325	-122.419
UW	YACT	BHZ	45.9325	-122.419
PB	B201	EH1	46.3033	-122.265
PB	B201	EH2	46.3033	-122.265
PB	B201	EHZ	46.3033	-122.265
PB	B202	EH1	46.2447	-122.137
PB	B202	EH2	46.2447	-122.137
PB	B202	EHZ	46.2447	-122.137
PB	B203	EH1	46.1690	-122.334
PB	B203	EH2	46.1690	-122.334
PB	B203	EHZ	46.1690	-122.334
PB	B204	EH1	46.1360	-122.169
PB	B204	EH2	46.1360	-122.169
PB	B204	EHZ	46.1360	-122.169
UW	ASR	EHZ	46.1526	-121.602
UW	CDF	EHZ	46.1169	-122.046
UW	EDM	EHZ	46.1972	-122.151
UW	ELK	EHZ	46.3054	-122.342
UW	FL2	EHZ	46.1962	-122.351
UW	GUL	EHZ	45.9240	-121.597
UW	HSR	EHZ	46.1743	-122.181
UW	JUN	EHZ	46.1471	-122.152
UW	LVP	EHZ	46.0659	-122.402
UW	MTM	EHZ	46.0253	-122.213
UW	TDL	EHZ	46.3507	-122.217

2.2 DLP EVENTS DETECTION

Because of the small size of the DLPs at MSH, only 22 events have been recorded in the PNSN catalog within the examined time window (Table 2.1). These events are characterized by relatively weak amplitudes, the largest reaching magnitude 1.3. They are deficient in energy above 10 Hz, and are reviewed, located and labeled long-period (or "low frequency") events by PNSN staff (Nichols et al., 2011; Vidale et al., 2014). To better assess the temporal activity of DLP events, we applied matched filter detection to continuous waveform data from Jan 2007 to Sep 2016, using all 22 events in the catalog as a template. We used 15 stations in total, including 3 three-component broadband stations, 4 three-component borehole short-period stations, and 8 one-component short period stations, all located within 30 km of the volcano (see Table 2.2 for station details). The 2007-2016 period represents the time window when the largest number of stations were operational, particularly the four borehole stations that have the lowest noise levels.

We first filter the template waveforms and the continuous waveform to a passband from 1 to 5 Hz, which is the dominant energy of the DLP events (see Figure 2.1 for example). For periods longer than 1 second, the signal is overwhelmed by the ambient noise, and there is less energy at frequencies higher than 5 Hz due to the source properties and wave attenuation.

We select a time window of 1 second before P arrival and 4 seconds after S arrival for the template, and perform cross correlation in the time domain for each channel. The average cross-correlation function, *C(t)*, is defined as

$$C(t) = \frac{1}{N}\sum_{1}^{N} c_i(t), \qquad (2.1)$$

in which *i* is the channel index (from 1 to 29), *N*=29 is the total number of channels, and c_i is the cross-correlation function for the i-th channel. If the average cross correlation is larger than a

threshold, then there is a consistent coherent signal similar to the template across all the channels, which we interpret as an event detection.

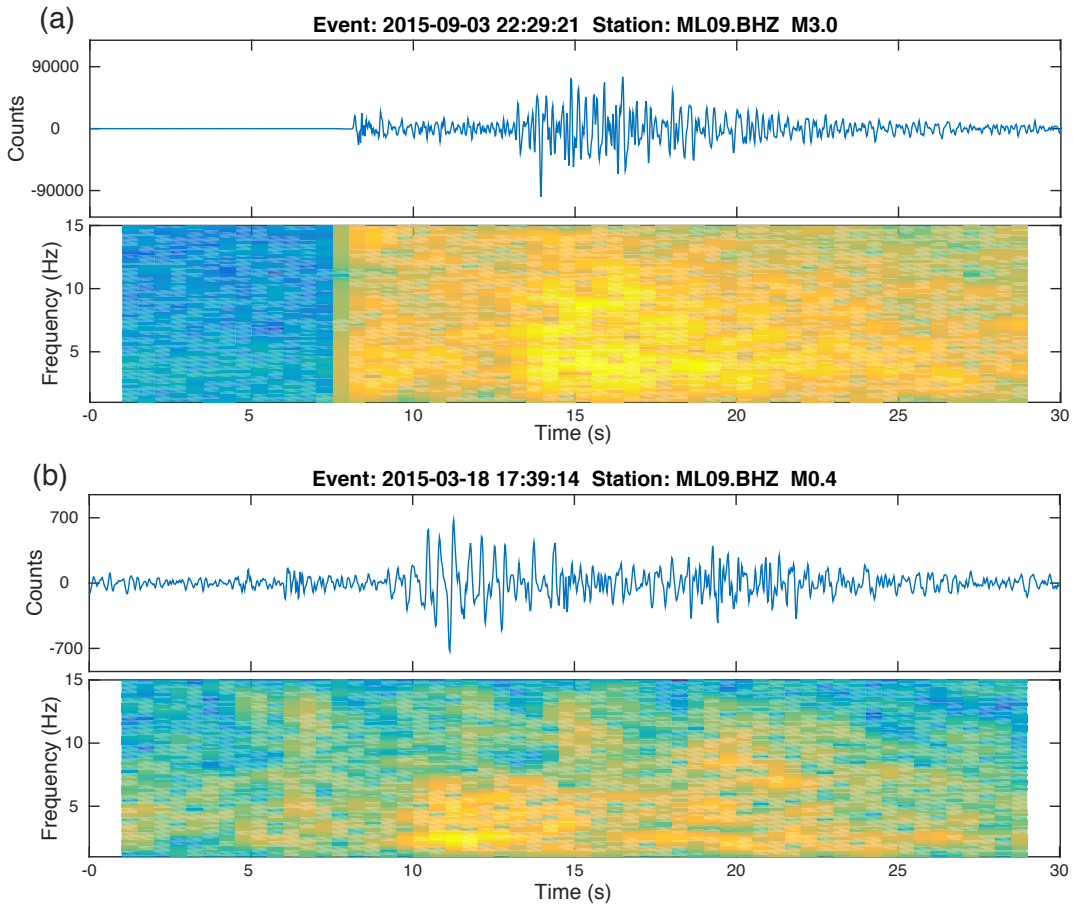

Figure 2.1. (a) Seismic waveform (top frame) and corresponding spectrogram (bottom frame) for a regular earthquake. (b) Same as (a) but for a DLP event. Note the scale change in counts for amplitudes.

The detection criteria are defined as: (1) at least 7 channels with data, and (2) an average cross-correlation function value greater than 10 times the standard deviation of the correlation function for that day (see Figure 2.2 for example). These criteria are considered conservative, and

there are hints of many more events just below detection. In Figure 2.3, we show the waveforms for some detected event examples.

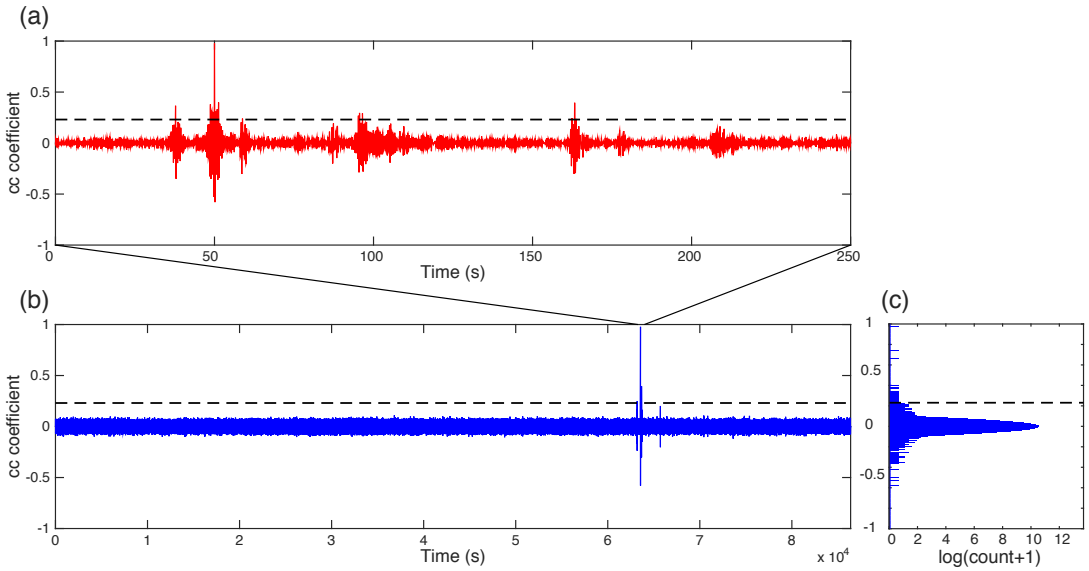

Figure 2.2. (a) Average cross correlation function showing a DLP swarm with four detected events in a window of 250 seconds. Gray dashed line is the threshold for detection. (b) A detection window of one day. (c) Histogram of the average cross correlation values.

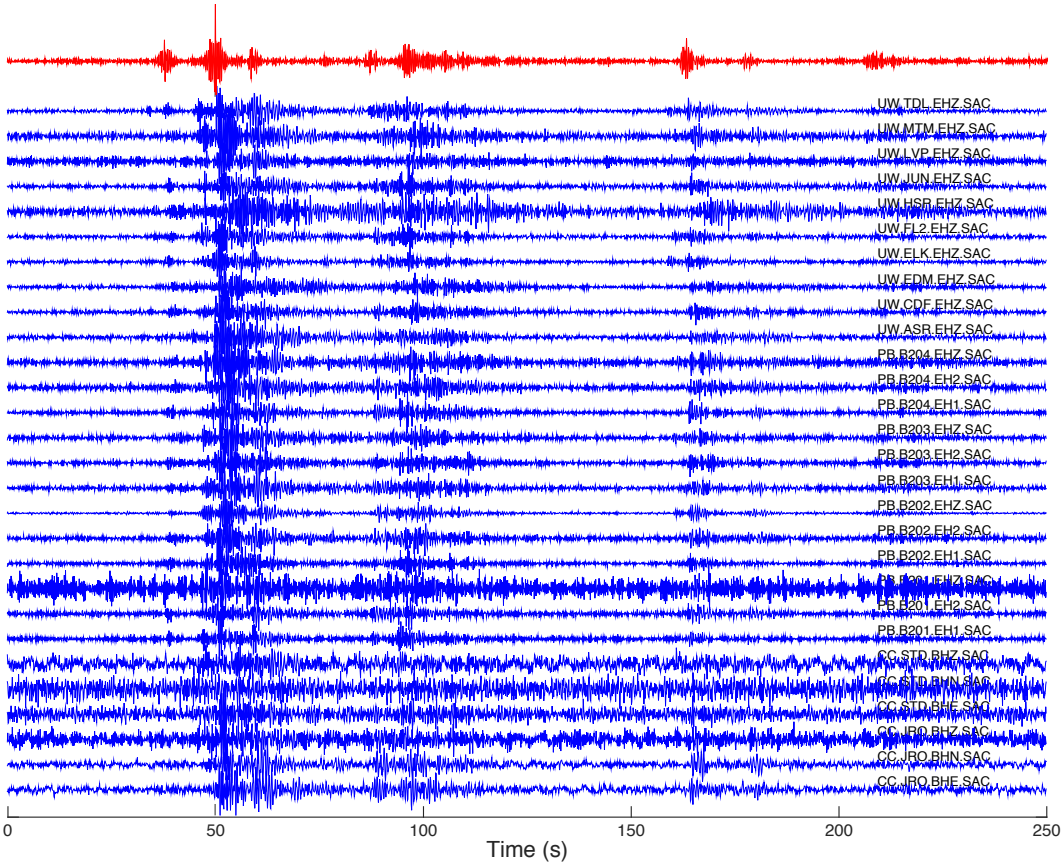

Figure 2.3. Waveform example for detected DLP events, with same time window as in Figure 2.2a. Red is the average cross-correlation function. Blue traces are the waveforms for all stations and channels.

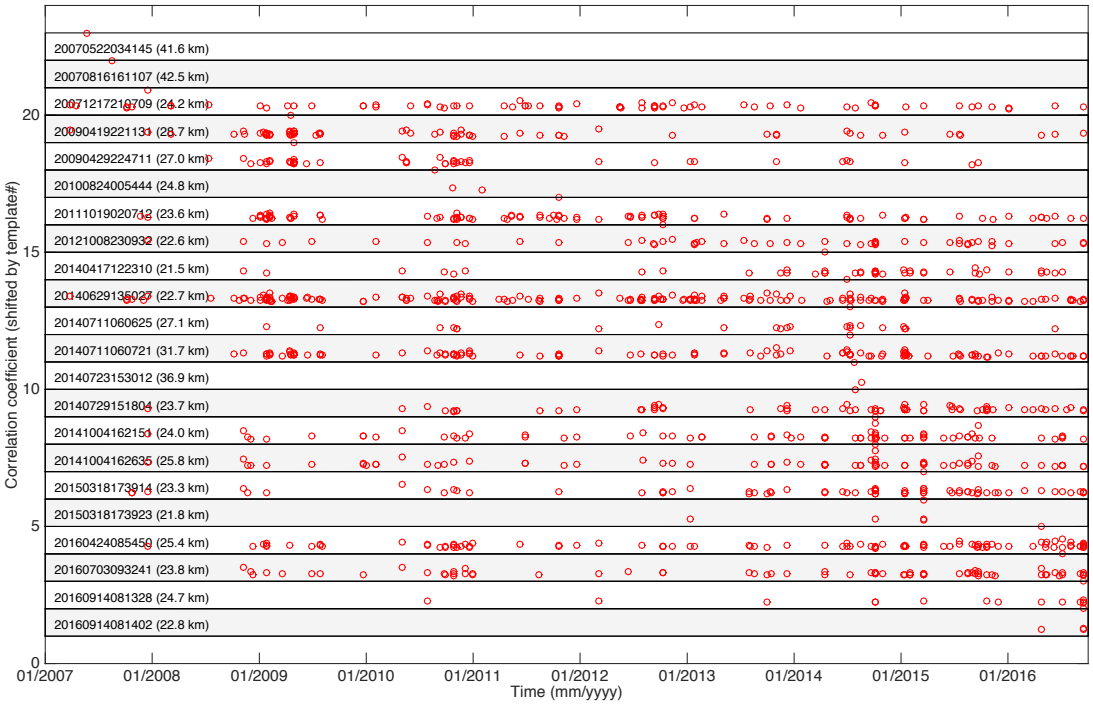

Figure 2.4. DLP detection for 22 template events with the detection results shown in separate rows.

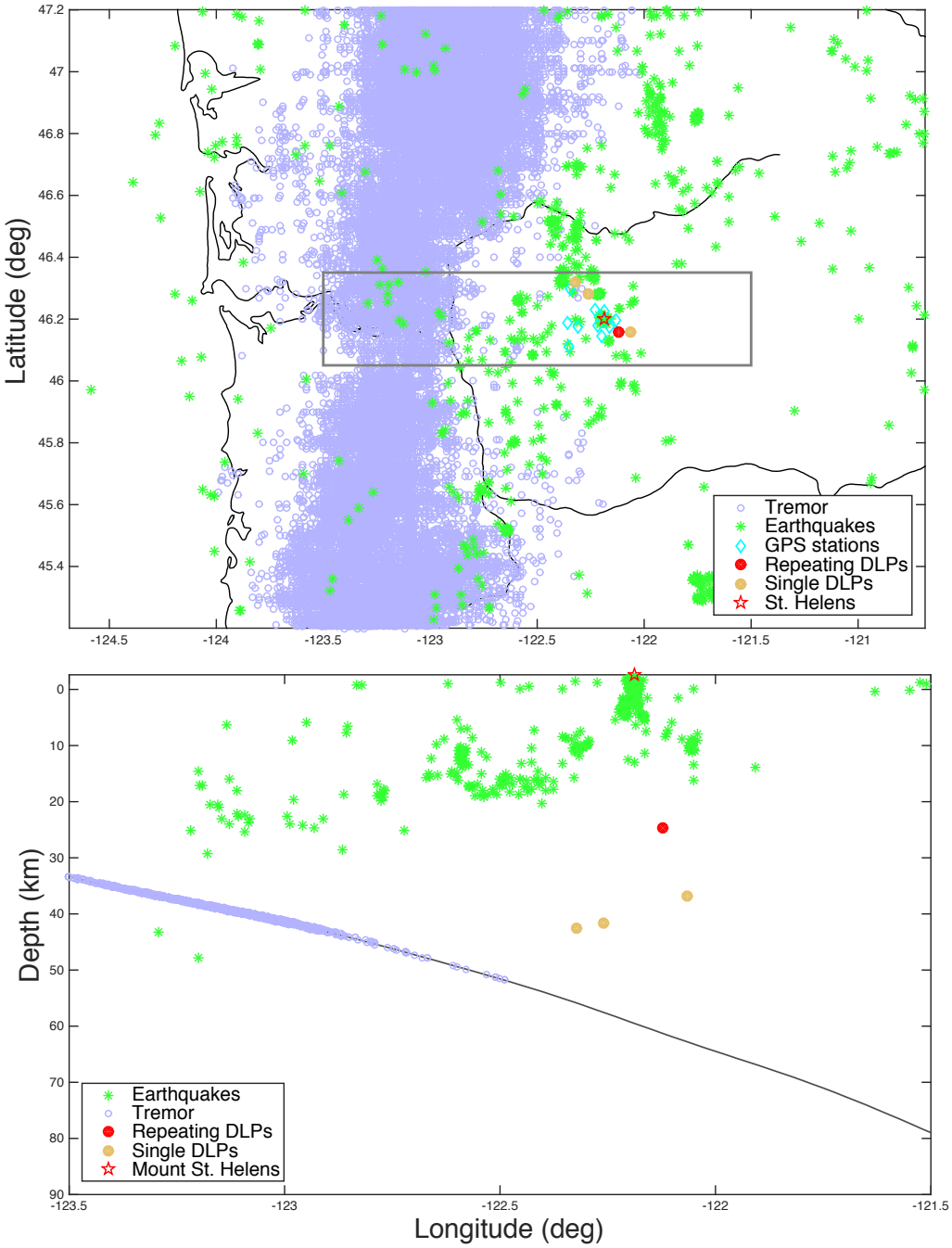

Figure 2.5. (top) Location map of background shallow seismicity (green), subduction zone tremor (blue), and DLPs near the Mount St. Helens volcano. (bottom) Cross section corresponding to the rectangle in top frame. Black line represents the subduction plate interface (McCrory et al., 2012).

DLPs at MSH fall into two categories, single DLPs and repeating DLPs (Figure 2.4 and Figure 2.5). There are only three single template DLPs observed in our study period. Two single DLPs (also reported by Vidale et al., 2014) are located northwest of MSH volcano; their depth indicates they occurred in the upper-most mantle (Figure 2.5). Dehydration embrittlement from an already hydrated mantle wedge has been invoked to explain their occurrence (Vidale et al., 2014). This possibility is also supported by low Moho reflectivity northwest of the volcano (Hansen et al., 2016). The third "single" DLP event, located southeast of the volcano, with a depth of 36.9 km, has only one detection in addition to the template itself. Given its depth and uncertainty, we are not sure if it occurred in the lower crust or the uppermost mantle. This DLP event might be associated with magma or fluid transport near the crust-mantle boundary.

All other DLP templates are repeating events with the same loci. We conclude this for two reasons. First, these templates detect each other and have very similar detection patterns in time (Figure 2.4). Second, they co-locate within 1 km, the resolution of cross-correlation location of these low signal-to-noise ratio (SNR) waveforms. All repeating DLP events are located to the southeast of MSH around a fast-to-slow seismic velocity boundary imaged from seismic tomography (Kiser et al., 2016). This boundary might represent the edge of a magma reservior, where fractures or cracks associated with magmatic or fluid processes would be found.

In the following sections, we analyze the effects of seismicity, ETSs, and tidal stresses on the repeating DLPs, as well as place constraints on their focal mechanisms.

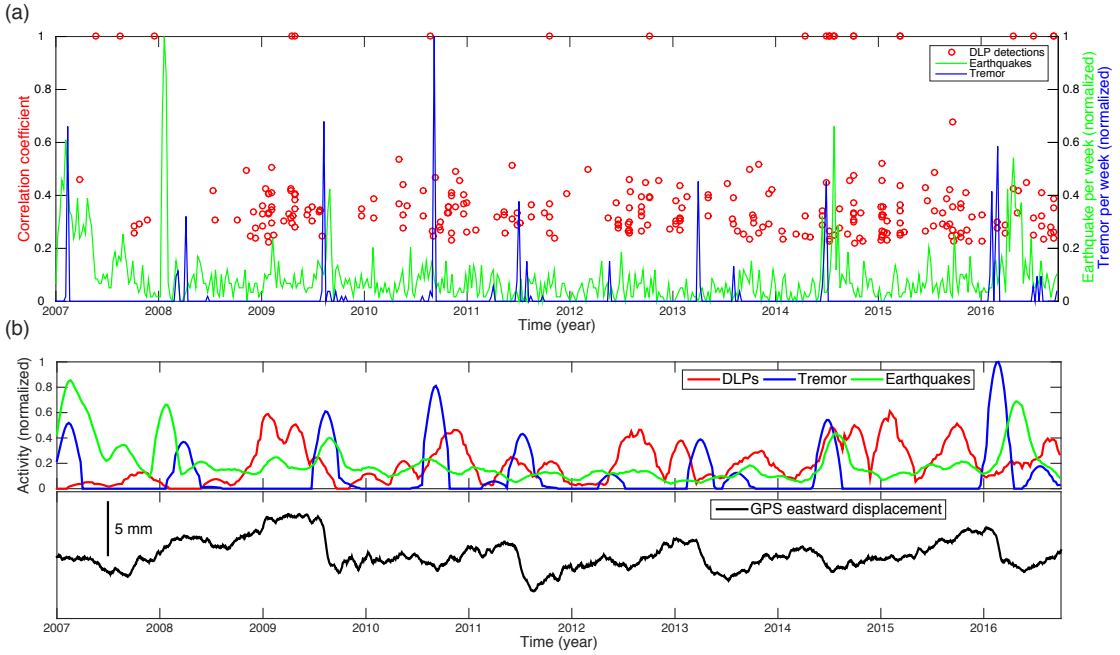

Figure 2.6. (a)Timeline of detected DLPs (red circles), subduction zone tremors (blue line) within a 100-km-wide band in latitude near the volcano, and shallow crustal earthquakes (green line) within 5 km of the volcano. (b) Same as upper figure but Gaussian smoothing applied with a three-month window. GPS (black line in bottom frame) is the average of eastward motion at 10 stations near Mount St. Helens.

2.3 No significant correlation between DLPs, ETS, and shallow seismicity

As one of the Cascade volcanoes, MSH volcano is located on the overriding plate of the Cascadia subduction zone. Episodic tremor and slow slip (ETS) events recur deep on the plate interface of the subduction zone, in a region located about 50 to 100 km west of MSH volcano. The deformation associated with ETS events might perturb the state of stress at the loci of those repeating DLP events enough to serve as a trigger. There is a conceivable connection between

these volcanic DLPs and the tremor activity at the subduction zone plate interface west of MSH through fluid movement or changes in fluid pressure. Therefore, we compared the timing of DLP activity with the tremor activity, as well as with slow slip recorded on GPS at MSH volcano (Figure 2.6).

In Figure 2.6b, we present the GPS displacement history at stations close to the volcanic center from 2007 to 2016, together with the DLP activity based on our detections and the tremor activity at the plate interface. Overall, the DLP events do show some long-term periodicity, although their periods are not as cyclic as ETS events. Unfortunately, with only a few ETS cycles, we do not observe a consistent pattern of activity. This observation serves to highlight ways these patterns should be tested more rigorously with more extensive catalogs. It is possible that a pattern may emerge as longer time histories become available in the future.

Also, if the ETS events at the subduction plate interface produce deformation big enough to cause the occurrence of the DLP events beneath MSH volcano, the deformation could also be large enough to affect shallow seismicity near the volcano. In such a scenario, the activity of the DLP events would show some connection with the shallow seismicity near the volcanic region. We checked the correlation between the shallow tectonic seismicity proximate to the volcano and the detected DLPs, but found no significant correlation (Figure 2.6). There is a tendency for shallow seismicity to peak near times of slow slip and tremor, although the peaks occur both just before (2007 and 2008) and just after (2009, 2014, and 2015) large ETSs, defying a simple explanation. In other words, neither shallow seismicity nor subduction zone ETS dependably triggers or results from processes associated with deep long-period events.

2.4 TIDAL MODULATION OF DLPS

The physical mechanism and driving forces of the DLPs is still unclear. DLPs are most often observed in volcanic areas, typically deeper than normal earthquakes, suggesting a connection to magmatic or fluid activity in a volcanic system (e.g., Aki and Koyanagi, 1981; Chouet, 2003). Their physical mechanisms in detail, however, have not been fully understood. If magma or fluid played an important role in the occurrence of the DLP events, their activities might, to some degree, be modulated by weak external driving forces such as stress perturbations from tides and surface waves during large earthquakes. To our knowledge, no previous tidal sensitivity of DLP events has yet been reported, while only tectonic tremor at subduction zones is observed to be strongly sensitive to tidal stress (Houston, 2015). This insensitivity could be due to the physical state beneath a volcano in general. The most recent activity of MSH is a major eruption starting in 1980, which renewed from 2004 to 2008 (Dzurisin et al., 2015). Therefore, MSH has an active flux of fluids from depth beneath the volcano. Due to weakness caused by the presence of fluids, seismic activity might be sensitive to small driving forces such as tidal stress.

Here, we shed some light on the physical mechanisms of DLP events by investigating their reaction to tidal stress modulation. In Figure 2.7, we present the correlation results between the timing of the DLPs and the amplitude of solid Earth tidal stress. We first calculate the tidal stress within the 10-year time window, sampled every 15 minutes. This sampling rate captures the diurnal tidal variation without aliasing. We compute the six-component stress tensor associated only with the solid Earth tide, neglecting the ocean tide; because MSH volcano is far from the ocean, the ocean tidal stress is much smaller than stress from the solid Earth tides. Then we count how many DLPs occurred at each tidal stress value, and also check the number of events expected if occurrence were random with respect to the tides. We compared the DLP activity with several

different individual components of the stress tensor from the tidal stress, and also various combinations of the components. We found the DLP activity shows greatest correlation with the volumetric component of the stress, the mean stress. From Figure 2.7, it is apparent that more DLP events are observed during the volumetric compressional phase of the mean tidal stress than would be expected with random occurrence. This correlation suggests that the mechanisms of these DLPs could be driven by magmatic and/or fluid activity, which would cause volumetric stress or strength perturbations.

Some detected DLPs occur in swarms (see Figure 2.6a), with several events occurring within an interval of seconds to tens of minutes. For tidal sensitivity analysis, we define a swarm as a cluster (with at least two events) in which each event in the cluster has at least one nearby event separated by less than one hour in time. 157 DLPs out of the detected 277 events are swarm events, in 55 DLP swarms (at least two events for each swarm). We found that the tidal correlation is even more significant for these swarm DLPs (Figure 2.8). This might be explained by a weakening mechanism of the system associated with fluid activities that have timescales shorter than the tidal timescale. Fluid activity will render the system more sensitive to tidal stress, and will also facilitate the occurrence of DLPs, so that when tide stress is encouraging, multiple DLPs occur in a time short relative to tidal stress changes.

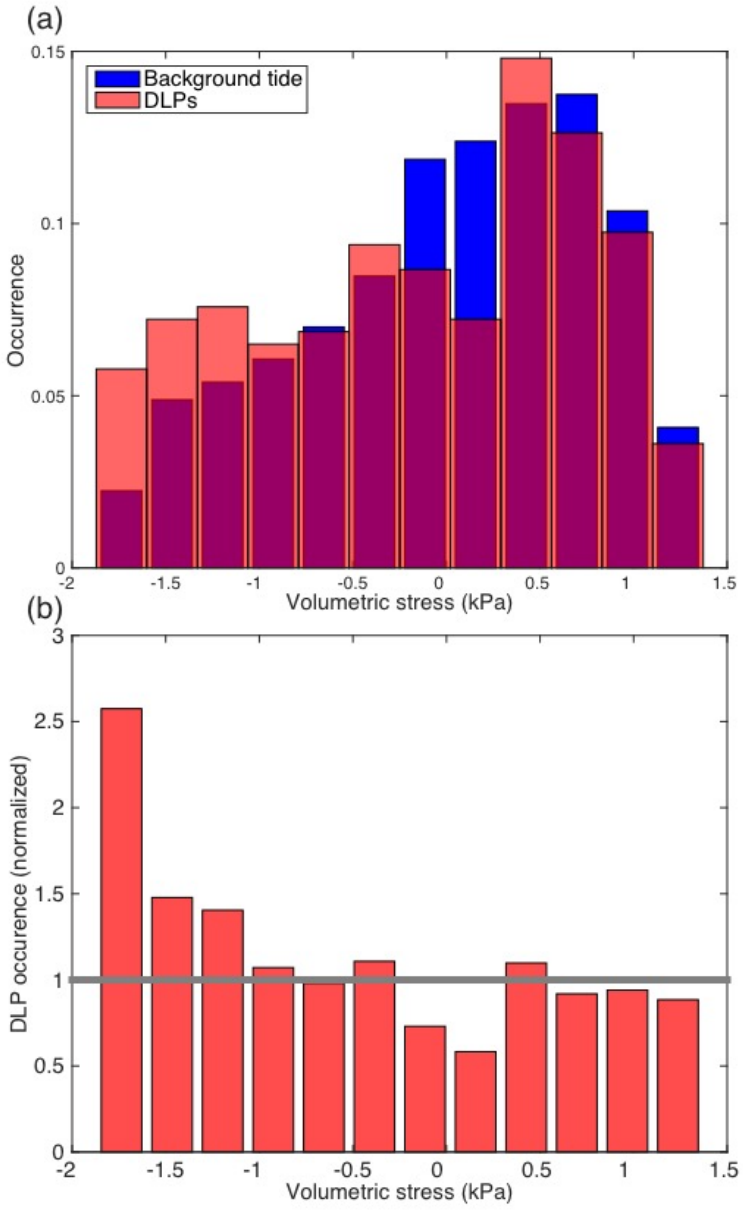

Figure 2.7. (a) Background tidal stress distribution (blue) and tidal stress distribution for DLP occurrence (red). (b) Ratio of DLP occurrence rate to portion of time at different tidal stress levels. The gray line represents the background level expected assuming random occurrence. More DLPs are detected during compressional mean tidal stress than expected at random.

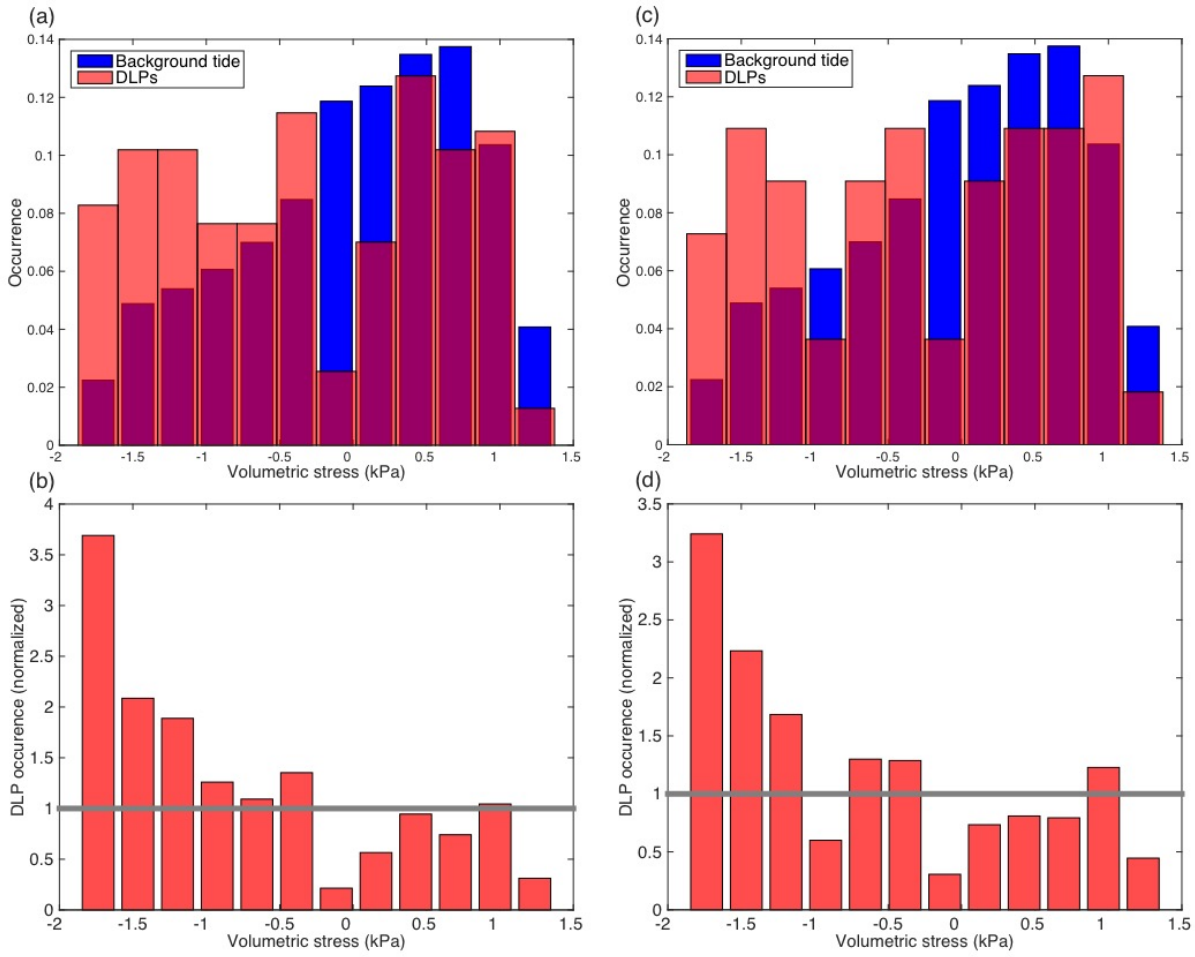

Figure 2.8. Same as Figure 2.7, but (a) and (b) use all 157 swarm DLPs, and (c) and (d) use declustered swarm DLPs (centroid timing of the 55 swarms).

We also checked the correlation between DLPs and large distant earthquakes, but no significant correlation was observed. Also, as previously stated, no significant correlation is observed between shallow earthquakes and DLPs. The stress loading period from the perturbation of the solid Earth tide is long compared to the dynamic stresses from earthquakes, either distant or local. The correlation of compressive stress seen at tidal periods apparently does not extend to the shorter periods at which large teleseisms exert their transient stresses. This pattern of stress sensitivity is distinct from tectonic tremor, which are observed to show sensitivity to long-period

tidal stressing (Houston, 2015), stress from distant surface waves (Rubinstin et al., 2008), and local small events (Han et al., 2014; Peng et al., 2009). Tectonic tremor has been inferred to occur via shear-faulting (e.g., Shelly et al., 2007). DLPs, however, might occur by a different physical mechanism, since they have a different stress perturbation sensitivity to exterior stress with different dominant periods, and are not located on known faults.

2.5 VARYING FOCAL MECHANISMS OF THE REPEATING DLPS

Focal mechanisms can provide insights on the physical mechanism of DLPs (e.g., Aso and Ide, 2014). The focal mechanisms of DLP events have been investigated in only a few cases (e.g., Aso and Ide, 2014). It is still not clear whether DLP events correspond to double-couple or other source mechanisms. Focal mechanisms are traditionally found from the polarity of the first P arrivals measured at many stations distributed around the focal sphere. Alternatively, for larger earthquakes, waveforms are used to invert for the moment tensor and the source time functions. A focal mechanism inversion for DLPs at MSH would be challenging due to (1) no or very weak P arrivals for most DLPs, thus no reliably picked polarities are available, (2) the frequency content concentrated between 1 to 6 Hz, depleted in higher frequency, thus arrivals not as sharp as regular earthquakes, (3) S arrivals with a long coda and a low SNR, (4) the complex velocity structure of MSH. It is difficult to obtain either reliable polarities or clean body waveforms to invert for the focal mechanism of the DLPs at MSH.

In this study, we analyze the particle motion of the initial S arrivals of DLPs to constrain their focal mechanisms. We only use the first 1.5 seconds of the S arrivals to measure particle motion polarization, to be less susceptible to waveform complications from scattered waves. Seismic data from the broadband iMUSH array are used to measure particle motions of DLPs. During the deployment of the iMUSH array (from July 2014 to August 2016), twelve DLP events were

recorded and their S arrivals are picked for particle motion analysis. We only used events and stations that have good SNR for quality control.

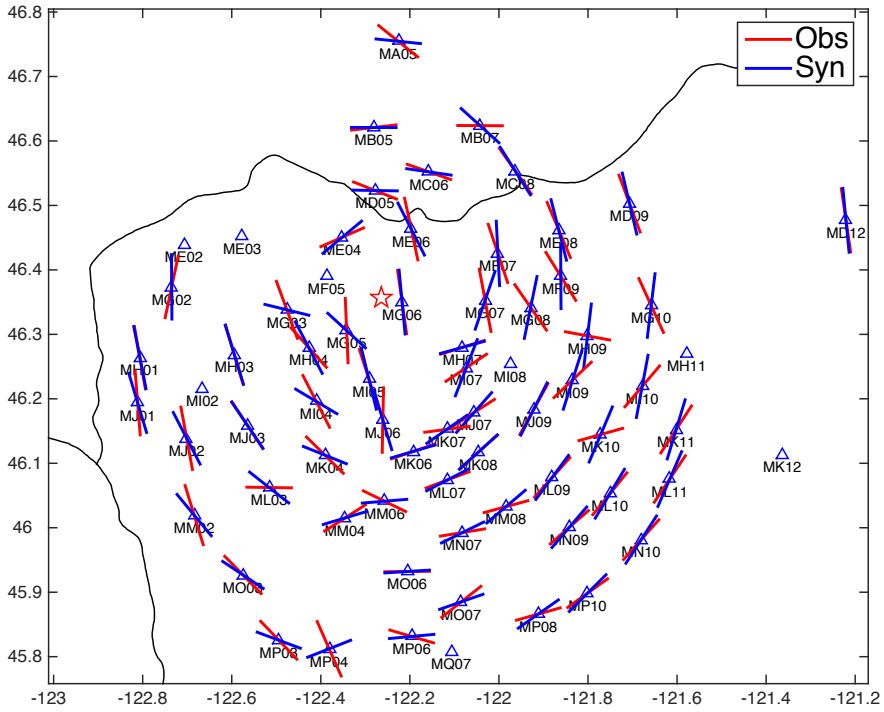

Figure 2.9. Particle motion polarization for an earthquake (09/03/2015 22:29:21, M=3.0, depth=11.5 km, strike=162, dip=76, rake=-117). Measurement window is the first 1.5 s of the S wave. Waveforms are filtered from 0.5 to 3 Hz. Red and blue bars represent polarization from observation and prediction from PNSN solution. Red star is the location of the earthquake.

We first measure the particle motion polarization for an earthquake event to check the technique (Figure 2.9). For each station, we filter the waveform between 0.5 Hz to 3 Hz, then calculate the 3x3 covariance from three-component waveform, select the eigenvector corresponding to the biggest eigenvalue, and finally project this eigenvector in the horizontal

direction. We also use the focal mechanism solution from the PNSN and one-dimensional velocity model to predict the S-wave polarization. It is apparent that the particle motion from the real observations is consistent with the prediction from the PNSN solution at most stations. We should note that only using S-wave particle motion polarization cannot uniquely determine the focal mechanism; for example, a reversed slip for a shear faulting source would produce the same polarization of particle motions.

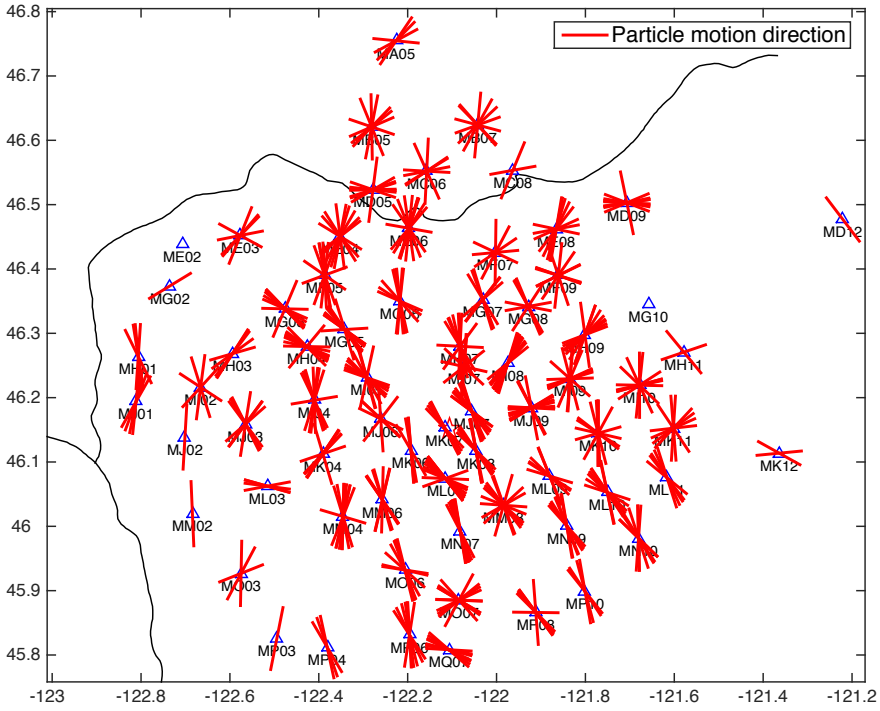

Figure 2.10. Particle motion polarization of DLP events. Measurement window is initial 1.5 s of S wave. Waveforms are filtered from 0.5 to 3 Hz. Blue triangles are iMUSH stations, and red bars are particle motion direction for DLP events.

We make the same measurement for DLP events, with results shown in Figure 2.10. The DLPs observed within the period of iMUSH deployment show a variety of different particle motion patterns. Therefore, they likely have differing focal mechanisms. Although the particle motion is different, the DLP locations are close to each other, as they detect each other based on the averaged waveform cross-correlation functions. We verified by grid searching of locations that many of the locations are within 1 km, the resolution of cross-correlation relocation of these low SNR waveforms. The varying focal mechanisms might be from either a differently-oriented crack plane or different combinations of components, including double couple, CLVD (compensated linear vector dipole), or volumetric component. There might even be a net force components evolved in the source, which has been attributed to unsteady flow of magmatic fluids (Ukawa and Ohtake, 1987; Miller et al., 1998). A close and continuous monitoring in the future with higher resolution of the focal mechanism in the future might be warranted, as the varying focal mechanisms could be related to the dynamic processes related to the hazard of the active MSH volcano.

2.6 Conclusions

With detailed analysis of ten years of data from the PNSN, supplemented by the iMUSH array, we detected 277 deep long-period earthquakes, with only 22 template events already in the PNSN catalog. We compare the DLPs' timing with that of ETS west of MSH volcano and with shallow seismicity, and find no robust correlation during our study period, although ETS and local earthquakes' timing may have some relation. The repeating DLPs southeast of the MSH volcano appear to correlate with the compressive mean stress in the solid Earth tides. The tidal modulation is found to be most significant for the DLPs that occurred in swarms, suggesting their occurrence might be associated with magmatic and/or fluid activity. The DLPs are observed to show varying

S-wave particle motion polarization. The varying particle motion polarizations might indicate diverse focal mechanisms, which could be due to dynamic interaction between the opening of fractures and movement of magmatic fluids.

2.7 References

Aki, K., and R. Koyanagi (1981), Deep volcanic tremor and magma ascent mechanism under Kilauea, Hawaii, J. Geophys. Res., 86, 7095–7109, doi:10.1029/JB086iB08p07095.

Aso, N., K. Ohta, and S. Ide (2011), Volcanic-like low-frequency earthquakes beneath Osaka Bay in the absence of a volcano, Geophys. Res. Lett., 38, L08303, doi:10.1029/2011GL046935.

Aso, N., and S. Ide (2014), Focal mechanisms of deep low-frequency earthquakes in Eastern Shimane in Western Japan, J. Geophys. Res. Solid Earth, 119, 364–377, doi:10.1002/2013JB010681.

Aso, N., and V. C. Tsai (2014), Cooling magma model for deep volcanic long-period earthquakes, J. Geophys. Res. Solid Earth, 119, 8442–8456, doi:10.1002/2014JB011180.

Chouet, B. A. (1996), Long-period volcano seismicity: Its source and use in eruption forecasting, Nature, 380(6572), 309–316.

Chouet, B., 2003. Volcano seismology. Pure and Applied Geophysics 160, 739–788. http://dx.doi.org/10.1007/PL00012556.

Dzurisin, D., S. C. Moran, M. Lisowski, S. P. Schilling, K. R. Anderson, and C. Werner (2015), The 2004–2008 dome-building eruption at Mount St. Helens, Washington: Epilogue, Bull. Volcanol., 77(10), 1–17, doi:10.1007/s00445-015-0973-4.

Hansen, S. M., Schmandt, B., Levander, A., Kiser, E., Vidale, J. E., Abers, G. A., & Creager, K. C. (2016). Seismic evidence for a cold serpentinized mantle wedge beneath Mount St Helens. Nature Communications, 7, 1–6. https://doi.org/10.1038/ncomms13242

Hill, D. P., P. Dawson, M. J. S. Johnston, A. M. Pitt, G. Biasi, and K. Smith (2002), Very-long-period volcanic earthquakes beneath Mammoth Mountain, California, Geophys. Res. Lett., 29(10), 1370, doi:10.1029/2002GL014833.

Houston, H. (2015), Low friction and fault weakening revealed by rising sensitivity of tremor to tidal stress, Nat. Geosci., 8, 409–415, doi:10.1038/ngeo2419.

Kiser, E. et al. Magma reservoirs from the upper crust to the Moho inferred from high-resolution Vp and Vs models beneath Mount St Helens, Washington State, USA. Geology 44, 411–414 (2016).

Matoza, R. S., P. M. Shearer, and P. G. Okubo (2014), High-precision relocation of long-period events beneath the summit region of Kilauea Volcano, Hawaii, from 1986 to 2009, Geophys. Res. Lett., 41, 3413–3421, doi:10.1002/2014GL059819.

McCrory, P. A., J. L. Blair, F. Waldhauser, and D. H. Oppenheimer (2012), Juan de Fuca slab geometry and its relation to Wadati-Benioff zone seismicity, J. Geophys. Res., 117, B09306, doi:10.1029/2012JB009407.

McNutt, S. R. (2005), Volcanic seismology, Annu. Rev. Earth Planet. Sci., 32, 461–491, doi:10.1146/annurev.earth.33.092203.122459.

Miller, A. D., G. R. Foulger, and B. R. Julian (1998), Non-double-couple earthquakes 2. Observations, Rev. Geophys., 36(4), 551–568, doi:10.1029/98RG00717.

Nichols, M. L., S. D. Malone, S. C. Moran, W. A. Thelen, and J. E. Vidale (2011), Deep long-period earthquakes beneath Washington and Oregon volcanoes, J. Volcanol. Geotherm. Res., 200(3-4), 116–128.

Power, J. A., S. D. Stihler, R. A. White, and S. C. Moran (2004), Observations of deep long-period (DLP) seismic events beneath Aleutian arc volcanoes; 1989-2002, J. Volcanol. Geotherm. Res., 138(3-4), 243–266.

Shapiro N. M., D. V. Droznin, S. Ya. Droznina, S. L. Senyukov, A. A. Gusev and E. I. Gordeev (2017), Deep and shallow long-period volcanic seismicity linked by fluid-pressure transfer, Nat. Geosci., 10, 442–445 (2017) doi:10.1038/ngeo2952.

Shelly, D. R., G. C. Beroza, and S. Ide (2007), Non-volcanic tremor and low-frequency earthquake swarms, Nature, 446, 305–307, doi:10.1038/nature05666.

Ukawa, M., and M. Ohtake (1987), A monochromatic earthquake suggesting deep-seated magmatic activity beneath the Izu-Ooshima Volcano, Japan, J. Geophys. Res., 92(B12), 12649–12663, doi:10.1029/JB092iB12p12649.

Vidale, J. E., D. A. Schmidt, S. D. Malone, A. J. Hotovec-Ellis, S. C. Moran, K. C. Creager, and H. Houston (2014), Deep long-period earthquakes west of the volcanic arc in Oregon: Evidence of serpentine dehydration in the fore-arc mantle wedge, Geophys. Res. Lett., 41, 370–376, doi:10.1002/2013GL059118.

CHAPTER 3. SEISMIC STUDY OF GROUND MOTION AMPLIFICATION IN SEATTLE BASIN

3.1 INTRODUCTION

The urban communities with large population in the Puget Sound area in Washington are exposed to potential earthquake hazards. First, megathrust earthquakes at the Cascadia subduction zone have ruptured every 300-600 years (with large uncertainties), and the last event occurred in 1700 (Wang et al., 2013). Another type of earthquakes are deep earthquakes, which occurred within the subducting Juan de Fuca slab, such as Mw 6.8 Nisqually earthquake (depth is 57 km) in 2001. The third category is shallow crustal events occurred in the overriding North American plate, and one example is the Seattle Fault rupture event which was estimated to have occurred about 1000 years ago (Atwater and Moore, 1992).

The city of Seattle sits atop a thick sedimentary basin, which can trap and amplify the seismic waves propagating across it. The shaking amplification in the basin could largely increase the shaking damage of earthquake and also magnify secondary hazards such like landslides. Therefore, the estimate of ground motion shaking is one of the central components to evaluate and mitigate the earthquake hazards in this area. Accurate estimate of the ground shaking would also provide useful information for other groups who are concerned with building construction and landslide hazards.

Ground motion estimation is often based on empirical regression of ground shaking observed in historical earthquakes (Toro et al., 1997). This estimate takes advantage of shaking measurements for real earthquakes and is fairly accurate for the potential events with the same location. This method is, however, limited by event distribution and numbers of historical earthquakes. For example, there is no previous instrumental recording of a magnitude 9 Cascadia

megathrust event, nor a Seattle fault event. Numerical simulations for scenario earthquakes have been commonly used to predict the shaking amplitude of ground motions (e.g., Frankel et al., 2009). Numerical simulations can capture wave propagation features such as focusing and amplification for seismic waves propagating across sedimentary basin, and thus are useful to evaluate the earthquake hazards. Earthquake numerical simulations require an accurate seismic velocity model as a prior, which rests on previous seismic structure studies and geophysical investigations. The velocity model, depending on the dataset it used, might suffer from limited accuracy and resolution.

The virtual earthquake method based on ambient noise cross correlation has recently been developed to predict earthquake ground motion (Prieto and Beroza, 2008; Denolle et al., 2014). This method has been applied to several basin area, for example the Los Angeles Basin (Denolle et al., 2014) and Kanto Basin in Japan (Denolle et al., 2014).

In this chapter, we use ambient noise cross correlation to retrieve the empirical green's functions (EGFs), which represent the seismic wave recorded at the receiver with point force imposed at the source location. There have been several previous studies using ambient noise correlation to study the velocity structure in regional scale in Washington (e.g., Calkins et al., 2011; Gao and Shen, 2014) and in Seattle basin (e.g., Delorey and Vidale, 2011). No previous studies have investigated the amplitude of the ambient noise and empirical green's function retrieved from noise correlation. To our knowledge, this is the first study that uses the amplitude information from ambient noise correlation to investigate the ground motion in Seattle basin. EGFs from ambient noise correlation in this study provide another independent and complementary estimate of the ground motion in Seattle basin, in addition to the estimate from historical earthquakes and numerical simulations. We also compare the relative amplitudes of EGFs with

ground motion amplitude observed from teleseismic S wave and from numerical simulations. By examining the similarity and discrepancy in EGFs and numerical simulation results, we attempt to cross validate the reliability of amplitude from EGFs and evaluate the accuracy and potentially can improve the velocity model used in earthquake numerical simulations in the future.

3.2 GROUND MOTION FROM NOISE CORRELATION

In the last decade new opportunities for seismic studies have arisen from examining the ambient seismic noise. Cross correlating the ambient seismic noise recorded at two stations would result in the so-called empirical (or estimated) green's function (EGF), which represents the expected ground motion at the receiver station in response to a point force at the source station (Lobkis and Weaver, 2001). The EGFs from ambient noise correlations have been extensively used to retrieve the phase information of surface waves, which are widely used in seismic tomography and seismic imaging to study the structure of the earth (e.g., Shapiro et al., 2005).

Amplitude information can also be extracted from ambient noise, although there is debate on the amplitude preserved in the noise correlation functions (Cupillard and Capdeville, 2010; Tsai, 2011; Prieto et al., 2011). Some studies (e.g., Prieto et al., 2011) show that stable amplitude information could be recovered for different time intervals, suggesting that the amplitude from noise cross correlations is useful with careful processing. A virtual earthquake approach has been proposed to exploit the amplitude information in EGFs from noise correlations to quantify the ground motion amplification in Los Angeles Basin (Prieto and Beroza, 2008; Denelle et al., 2014) and in Kanto Basin (Denelle et al., 2014). Through appropriate process of ambient noise data and cross correlation calculation of ambient noise at two separated stations, the amplitude from the EGFs can be retrieved and used to estimate the ground motion amplification across the basin.

3.2.1 Data and method

We use seismic data from 15 stations from the Puget Sound broadband array (Creager and Malone, 1996). This is a linear array stretching from the Olympia Mountains to the west across the Seattle basin to the Cascade Mountains to the east (Figure 3.1). All stations are three-component (CMG sensor) with a sampling rate of 20 samples per second, and were operated from February to April for a period of about 85 days in 1994.

We briefly introduce the theoretical background on the theory and method of noise cross correlation, more detailed background can be found in many previous theoretical and applied studies (e.g., Lobkis and Weaver, 2001; Prieto and Beroza, 2008; Tsai, 2011). Assume that we have two stations A and B, which are treated as a source station and a receiver station, respectively. The cross correlation of the ambient noise recorded at these two stations can be expressed as (in frequency domain),

$$C_{AB}(\omega) = u_A(\omega)u_B^*(\omega), \quad (3.1)$$

where ω is frequency, u is displacement, * represents conjugate, and C is the cross correlation function (in frequency domain). Under certain conditions, the derivative of the cross correlation function is proportional to the green's function between the two stations. To relate the cross correlation function to the green's function, the ambient seismic field is required to be stationary and noise energy should be spatially homogeneous. However, in real applications, these conditions are not necessarily satisfied. There are previous studies which show that the ambient noise energy show seasonal directivity, for example in California (Stehly et al., 2006) and in the Pacific Northwest (Tian and Ritzwoller, 2015). The azimuthal content and seasonal variation of the ambient noise field are also frequency-dependent (e.g., Stehly et al., 2006; Tian and Ritzwoller,

2015). All these issues should be taken into account when using ambient noise correlation to retrieve and interpret the amplitude of the empirical green's functions.

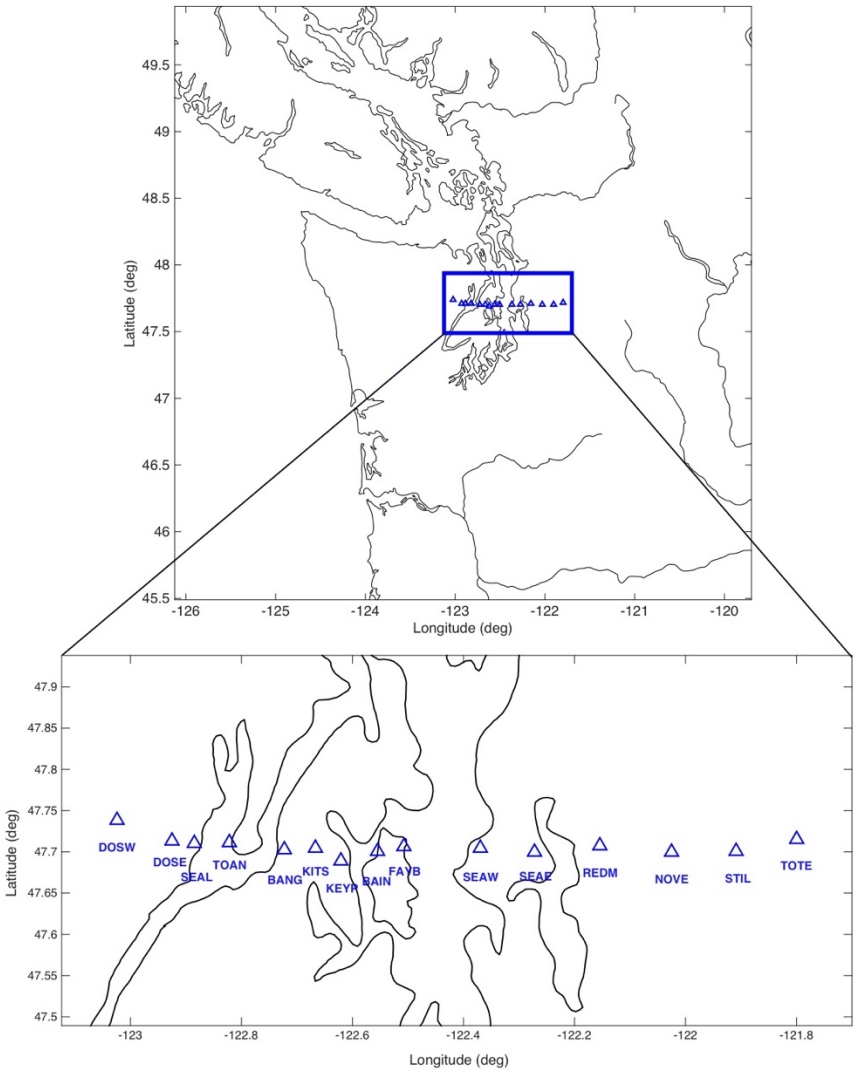

Figure 3.1. Puget Sound broadband array consist of 15 stations (blue triangles), which stretch across the Seattle basin from Olympia Mountains to the west to Cascade Mountain to the east.

Following previous studies (e.g., Benson et al., 2007; Prieto et al., 2011; Denolle et al., 2011), we mainly apply two techniques of data processing for ambient noise data, which both partially

mitigate potentially unsatisfactory conditions of the ambient noise field. First, we cut the continuous ambient seismic noise data into segments with a time window of 30 minutes. We discard those windows that have very large amplitude (8 times of the standard deviations of the data for the day), such that some anomalous spikes, for example teleseismic signals, are ignored. We perform cross correlation calculation for each time window, then stack the correlations for all segments within the total 85 days.

The other method we have applied for data processing is normalization. Normalization can be done in time domain for ambient seismic noise data, for example using one-bit clipping (Benson et al., 2007; Prieto et al., 2011). Especially, one-bit normalization in the time domain is commonly used in applications that measure travel time from noise correlation functions, since this method does not change the phase information. One-bit normalization changes the amplitude information of the ambient noise field and thus the amplitude retrieved from empirical green's functions (Prieto et al., 2011), although some study shows that the amplitude information can (at least partially) be preserved even with one-bit normalization (Lin et al., 2011). Another category of normalization is spectral normalization, which is done in the frequency domain before correlation. In this study, we apply the spectral normalization in the frequency domain based on the following equation (Prieto et al., 2011; Denolle et al., 2013),

$$H_{AB}(\omega) = < \frac{u_A(\omega) u_B^*(\omega)}{|u_A(\omega)|^2} >, \qquad (3.2)$$

where u is displacement, H is the transfer function, the brackets represent ensemble average (stacking over time windows). The function in the time domain corresponding to H(ω) is called an impulse response function (IRF). In equation (3.2), the denominator is the spectral power of the source station A. Some studies also use the spectra of both source station A and receiver station B as the denominator for normalization, which is equivalent to spectral whitening (Benson et al.,

2007; Prieto et al., 2011). In this study, we use ambient noise data to calculate the transfer function following equation (2), and then we get the IRF, which is used as an EGF to retrieve and interpret the amplitude of the seismic wave propagating from source station A to receiver station B. In computation, we apply spectral smoothing for the source station A and apply water level to avoid the instability of the deconvolution in equation (2). We do the same data processing and cross correlation for all station pairs. In this study, we choose periods from 5 sec to 10 sec, and only use vertical components to compute noise correlation, so Rayleigh surface waves would be observed but not Love wave.

3.2.2 Noise correlation results

In Figure 3.2, we show the noise correlation waveforms, which are calculated by using station DOSW in Olympia Mountain as the source station and all other stations of the linear array as receiver stations. The waveform amplitudes in Figure 3.2 are corrected by a factor of square root of distance to take into account the geometrical spreading, so amplification effects are more easily visually quantified. Signals with move-out velocity between 1 km/s and 3 km/s are observed, and the apparent velocity suggests they are mainly surface waves.

3.2.3 Uncertainties

The accuracy of the EGFs from ambient noise correlation depends on the characteristics of the ambient noise field. In some situations, the calculated correlation function might be significantly biased from the true green's function. For example, if the noise source is not homogeneously distributed, both the phase and amplitude of the noise correlation function can be biased. This bias mainly depends on the azimuthal pattern of the noise energy. In this study, the data we have used is from Puget Sound broadband array, which is a linear seismic array. Therefore, the azimuthal

heterogeneity of the seismic noise energy might not be a big issue when considering the uncertainties in the noise correlation results. We note that all observations in noise EGFs should only represent measurements in west-east direction. Ground motion amplification may show different variation pattern with incoming source from north or south. The influence of noise azimuthal variations on noise correlation in Seattle basin should be investigated in the future.

Another issue is that the ambient noise field might not be stationary. Alternatively, the ambient noise field might show temporal variations, for example seasonal variations. Previous studies have shown that the ambient noise source is mainly generated from the interaction between the atmosphere, ocean and sea floor, and the noise energy directivity show seasonal variation pattern (e.g., Stehly et al., 2006). Equivalently, ambient noise field with seasonal variations would result in spatial heterogeneity for the noise source. The data we used in this study span a relatively short period (from February to April), and thus the ambient noise field may not be expected to vary very much. We validate this assumption by checking the temporal change of the cross correlation functions. As shown in Figure 4, we find the daily noise correlations have only very small variation. Within this time window, the noise correlation functions generally show consistent results both in phase and amplitude. For the same station pair, the correlation function might vary during other time period of the year. It could be useful to use longer time window to calculate the empirical green's function, in order to reduce the bias from source heterogeneity.

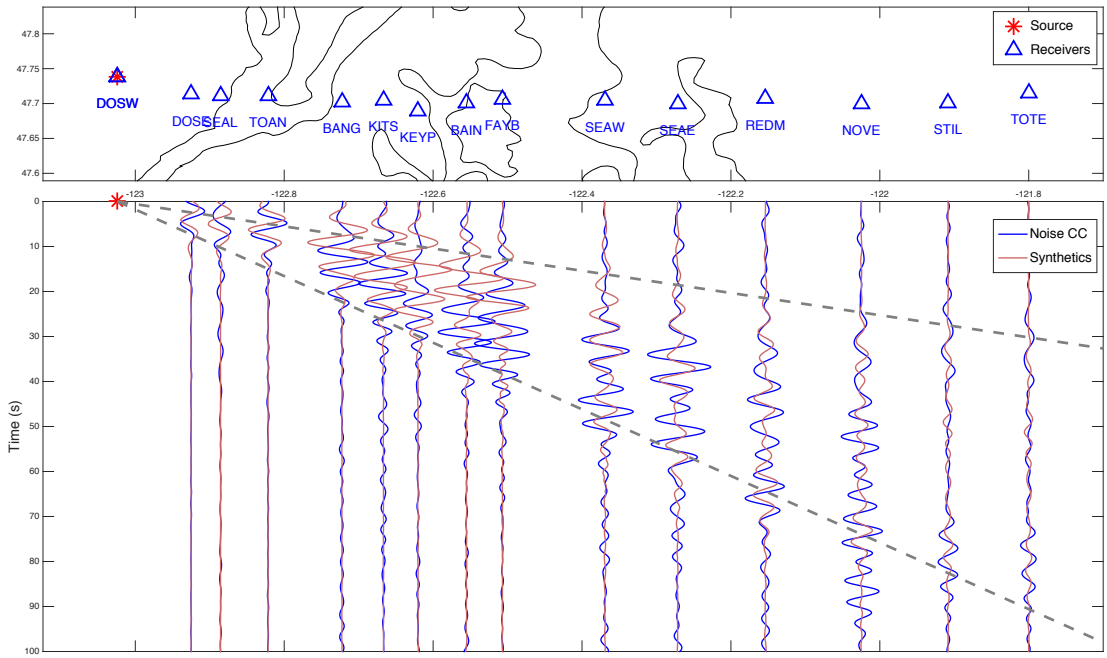

Figure 3.2. (top) Station distribution of the Puget Sound broadband array. Blue triangles are stations, while the red asterisk is the source station. (bottom) Waveforms from noise cross correlation (blue traces) and synthetic waveforms (red traces). The most westward station DOSW is taken as the source station and all other stations as receiver stations in calculating noise cross correlation. All waveforms are filtered between 5 and 10 seconds. Two gray dashed lines represent wave propagation with moveout velocity of 3 km/s and 1 km/s, respectively.

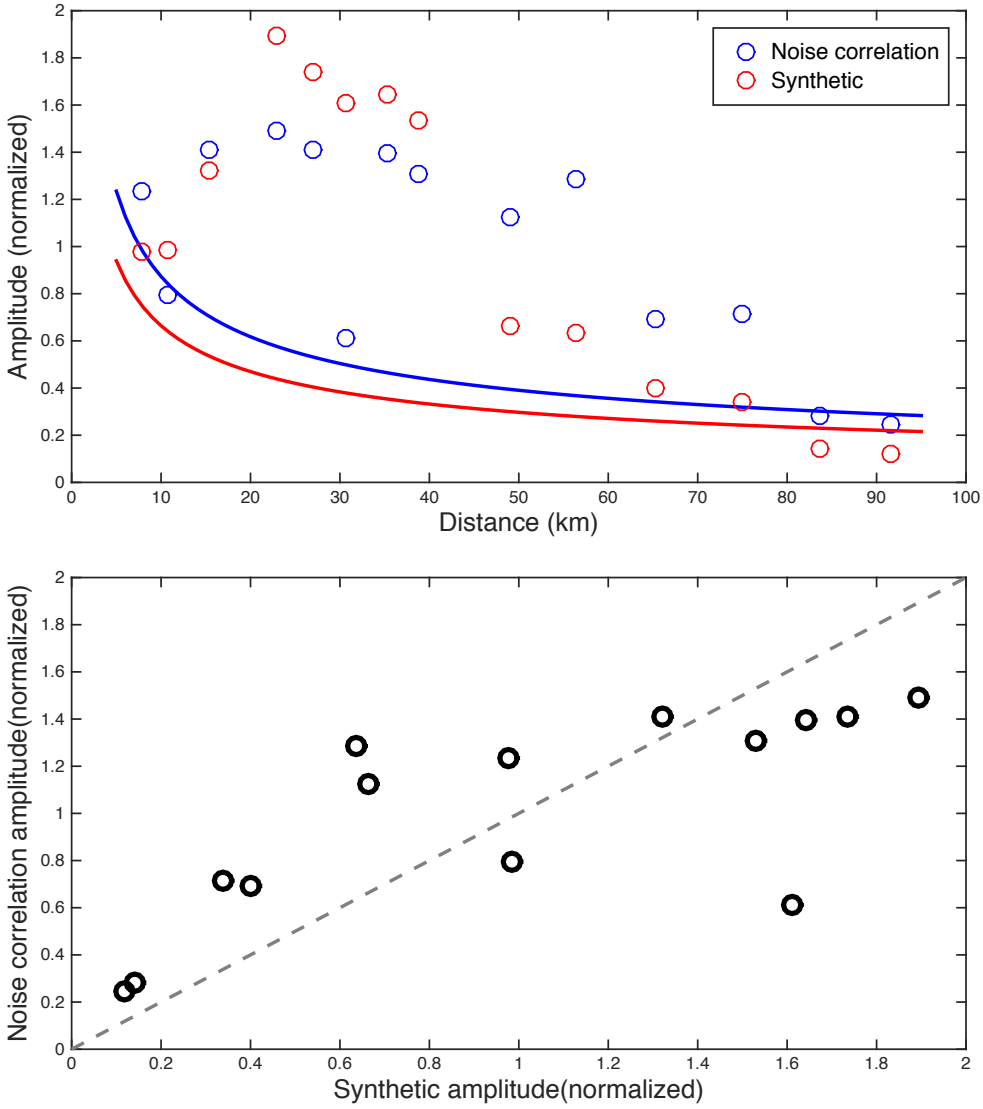

Figure 3.3. (top) Amplitude measured from noise correlation functions (blue) and synthetic waveforms (red). Two solid lines represent the geometrical spreading with factor of $1/\sqrt{r}$, where r is distance from source to receiver. These two lines are determined by fitting the amplitudes from two stations from Olympia Mountains and two stations from Cascade Mountains. (bottom) Comparison between amplitudes measured from noise correlation EGFs and those measured from synthetic waveforms.

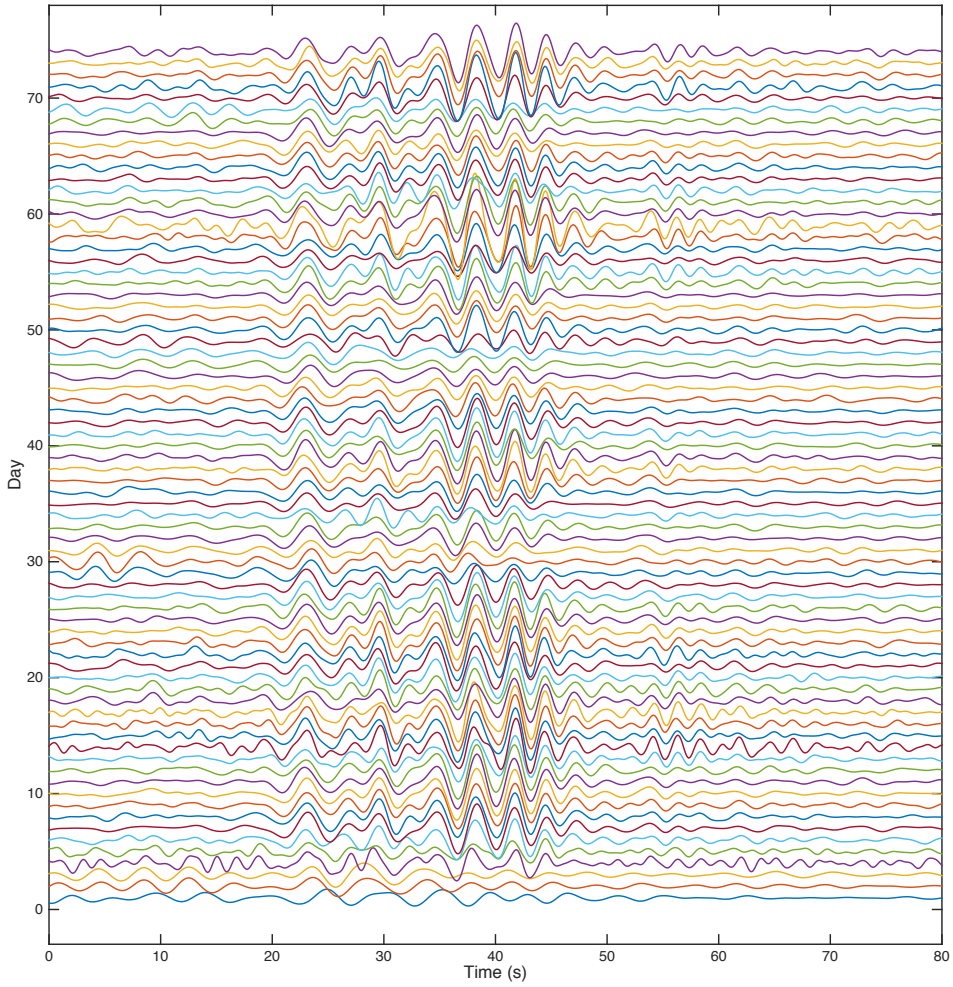

Figure 3.4. Temporal variation of the cross correlation for station DOSW (located in Olympia Mountain) and station FAYB (located in Seattle basin). Each trace represents the calculated the cross correlation using data from one day.

3.3 AMPLITUDE OF TELESEISMIC S WAVE OF DEEP FIJI EARTHQUAKE

In this part, we examine the ground motion response across Seattle basin from large teleseismic earthquake recorded on the Puget broadband array (Figure 3.5). Teleseismic data have been widely used to investigate the velocity structure beneath the receivers. The most commonly used method is receiver function, which uses a deconvolution technique to invert for the velocity structure below

the stations. Our purpose in this study is to quantify the ground motion amplifications in the basin, so we directly measure the S wave amplitudes from the teleseismic earthquake rather than using deconvolution. Also, we compare the amplitudes of the teleseismic S wave with those measured from noise EGFs, such that we can cross validate the amplifications from both dataset and methods.

The Mw 7.6 Fiji deep earthquake, which occurred on March 9, 1994, was well recorded by the Puget Sound broadband array and provides good signal-to-noise (SNR) data to investigate the ground motion amplification across the Seattle basin. This is a deep-focus event, which minimizes the complexity of the source side scattering. Both P and S waves are well recorded by the seismic array (Figure 3.5). We pick the P and S arrivals, and measure the amplitude after filtering the waveforms between 5 sec to 10 sec, so we could also compare them with those measured from noise EGFs.

From the waveforms and measurements, two main features can be identified. First, for both the P arrivals and S arrivals, the amplitudes in Seattle basin are larger than those at mountain area. The shaking amplitude of S wave within the basin is amplified by almost a factor of 3, compared with that in Olympia and Cascade mountains (Figure 3.5, Figure 3.6). Another apparent feature is that the Seattle basin traps seismic wave and thus has persistent ground shaking even several minutes after the direct incoming waves. The teleseismic wave are nearly vertically incident beneath the array, and the thick sedimentary deposit with low velocity plays the key role in amplifying the ground motion amplitudes. The thicker the sediment basin and lower velocity and density, the larger the impedance contrast with the basement rock, and thus the larger the amplitude of ground motion.

The propagating waves retrieved from noise cross correlation are mainly surface waves, which propagate horizontally. The amplitude of surface wave is also very sensitive to the shallow structure of the medium it is traversing. We compare the amplitude measured from ambient noise EGFs and those measured from teleseismic S wave (Figure 3.6). In general, these two independent measurements show a consistent spatial pattern. Ground motions in Seattle basin are larger than those in mountain area, amplified by a factor of 2 to 3. Again, this amplification factor only represents for the scenario with waves propagating from west to east. This consistency suggests that the EGFs we retrieved from ambient noise cross correlation preserves the amplitude information, including geometrical spreading, attenuation, and site amplification. Future work may be needed to quantify these different components with data from more stations and longer duration.

3.4 COMPARE EGFS WITH NUMERICAL SIMULATIONS

Numerical simulations complement other methods in ground motion study by providing estimate for scenario earthquakes without limitations of station availability (e.g., Frankel et al., 2009). Previous simulations (e.g., Frankel et al., 2009) captured most of the important basin effects seen in real observed earthquake seismograms, such as amplification, observed basin surface wave and the focusing of S wave at the basin edge. Also, amplification, and possibly other features, depends on the direction of the earthquakes. In this section, we apply numerical simulations with specified source to calculate synthetic waveforms, which then are used to compare with empirical green's functions based on noise correlation. With such comparison, we attempt to cross validate both the reliability of the noise EGFs and the velocity model used to compute synthetics. We note that ultimately the amplitude of EGFs can be used to refine the current velocity model in the future.

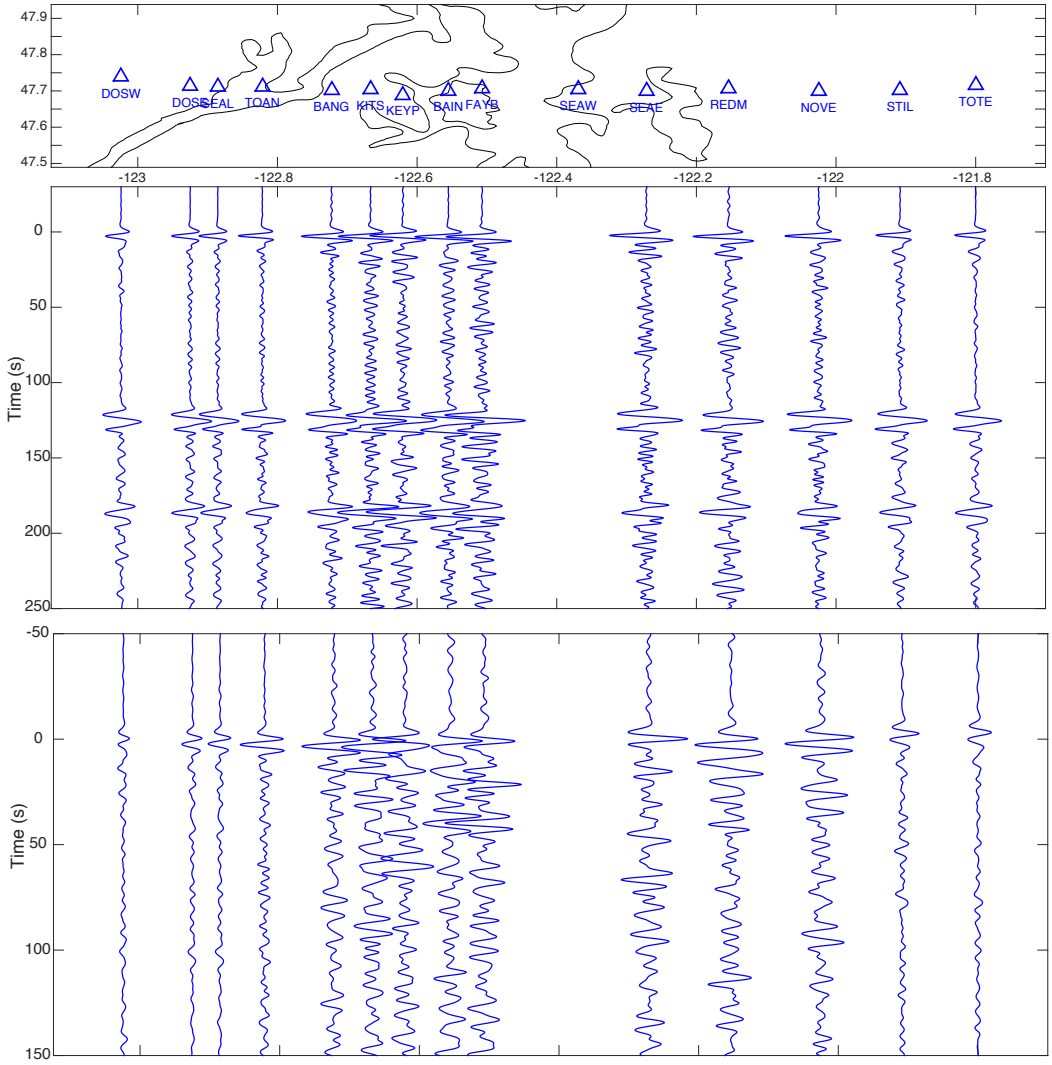

Figure 3.5. Teleseismic waveform of the 1994 deep Fiji earthquake recorded by Puget Sound broadband array. (top) Map view of station distribution. (middle) Three phases are P, pP and PP, respectively. (bottom) S wave. Waveforms are filtered between 5 sec and 10 sec.

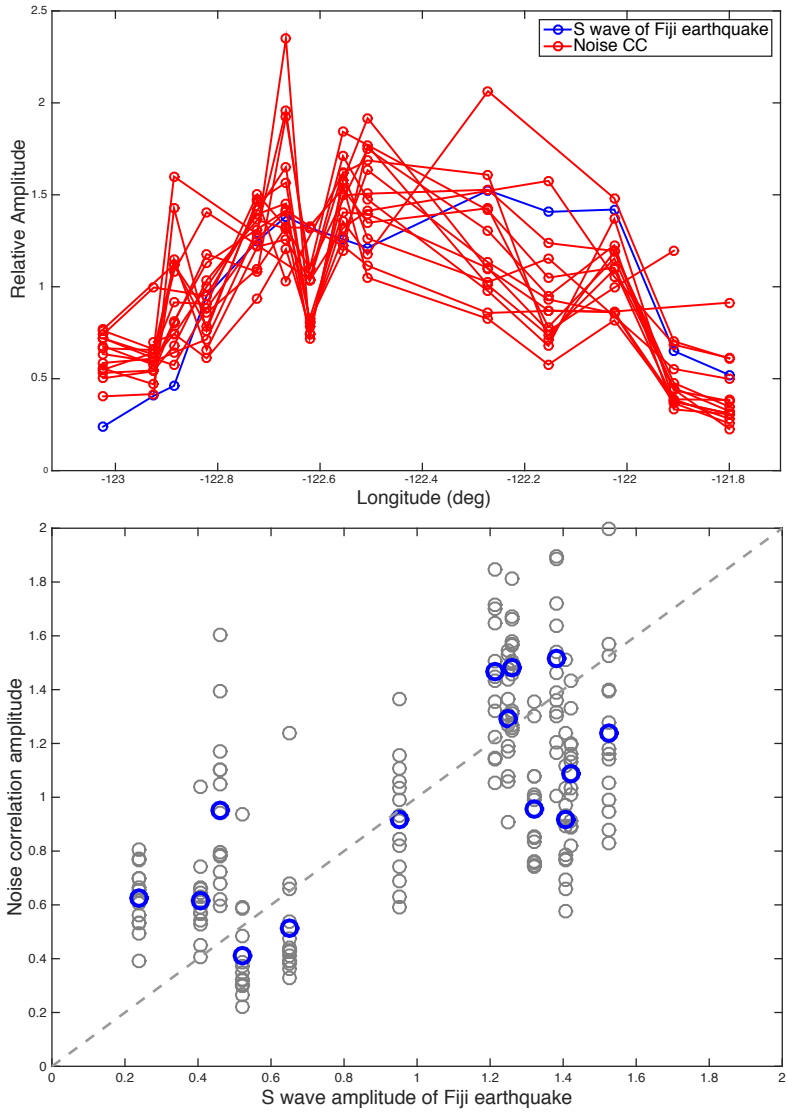

Figure 3.6. (top) Amplitude (normalized) variations as observed from teleseismic S wave from deep Fiji earthquake (blue) and measured from the noise correlations. For noise correlations, each receiver station has multiple measurement from other source stations. (bottom) Direct comparison between S wave amplitude of Fiji event and amplitude from noise correlations. Gray circles represent individual measurements from station pairs and blue are amplitude averaged with respect to receiver stations. Gray dashed line means these two measurements are equal to each other.

To calculate the synthetic waveforms, we apply the 3D finite-difference program (Liu and Archuleta, 2002) with a defined velocity model. The velocity model used to calculate the synthetics is constructed for Puget Sound and Pacific Northwest from multiple dataset from seismological, geophysical and geological studies, and has been described in previous work (Stephenson, 2007; Frankel et al., 2009). The details of model configuration and numerical parameters for simulations can also be found in earlier studies (see Frankel et al., 2009).

The EGF corresponds to the observed seismogram with an imposed point force. Synthetic simulations should also specify a point-force source, to enable a direct comparison with EGFs. The source input of the finite-difference program is a double couple (or moment tensor), which is also the type of source we used in our simulations. Calculating synthetics with point-force source is still ongoing work and has not been completed yet. In the rest of this chapter, we only show and discuss synthetics from double-couple source. We specify the source with a compensated linear vector dipole (CLVD), with the symmetric axis in vertical direction, by adding two double couple source. This CLVD source is similar to a vertical force in that they both have a symmetric axis in the vertical direction, and they both do not generate Love wave.

Synthetic waveforms are shown in Figure 3.2, which are compared with EGFs from ambient noise correlation. In general, they are comparable with each other, both in waveforms and in amplitudes (Figure 3.2, 3.3). Both amplitude patterns reflect geometrical spreading and focusing effect across the profile (Figure 3.3a). Their consistency suggests that the amplitude observed from ambient noise EGFs contains reliable information, which can be interpreted in terms of geometrical spreading, attenuation, and amplification. Notable discrepancies, however, are found at western Seattle basin. Synthetics appear to have earlier arrivals and higher amplitudes than

observed on noise EGFs. One possible reason is that EGF from noise correlation only capture surface wave but not body wave. In simulations, especially at short distance, the superposed body wave would contribute to both earlier arrivals and larger amplitudes. Alternatively, the earlier arrivals seen in simulations might be due to an inaccurate velocity model, which might be too fast to capture the delayed waves seen in the cross-correlation seismograms. However, we don't see earlier arrivals on synthetics for further stations to the east, which might be due to slow velocity for eastern part of the basin compensating the fast velocity to the west in the model. This interpretation suggests the potential usage of EGFs to improve the current velocity model.

3.5 Conclusions

Using seismic data from Puget Sound broadband array, we retrieve empirical green's function based on ambient noise cross correlation. The amplitudes measured from noise EGFs provide independent estimate on ground motion amplification in Seattle basin. Consistent amplitudes from noise EGFs, teleseismic S wave and synthetic simulations, and stationary characteristics of EGFs all suggest the usefulness of the amplitude of EGFs. For wave with period of 5-10 sec propagating from west to east across the basin, the ground motion is amplified by a factor of up to 3 within the basin compared with mountain regions. The discrepancy might be due to either the uncertainty (bias) of EGFs from noise heterogeneity or inaccuracy of the velocity model used in numerical simulations, both are still to be investigated.

3.6 Reference

Atwater, B. F., and A. L. Moore (1992), A tsunami about 1000 years ago in Puget Sound, Washington, Science, 258(5088), 1614-1616, doi:10.1126/science.258.5088.1614.

Benson, G.D., Ritzwoller, M.H., Barmin, M.P., Levshin, A.L., Lin, F., Moschetti, M.P., Shapiro, N.M. & Yang, Y., 2007. Processing seismic ambient noise data to obtain reliable broad-band surface wave dispersion measurements, Geophys. J. Int., 169, 1239–1260.

Calkins, J. A., G. A. Abers, G. Ekström, K. C. Creager, and S. Rondenay (2011), Shallow structure of the Cascadia subduction zone beneath western Washington from spectral ambient noise correlation, J. Geophys. Res., 116, B07302, doi:10.1029/2010JB007657.

Creager, K. C. and S. D. Malone (1996), Broadband Array Analysis of the Puget Sound Region. USGS Final Technical Report.

Cupillard, P., and Y. Capdeville (2010), On the amplitudes of surface waves obtained by noise correlation and the capability to recover the attenuation: A numerical approach, Geophys. J. Int., 181, 1687–1700.

Delorey, A.A., Vidale, J.E., 2011. Basin shear-wave velocities beneath Seattle, Washington from noise-correlation Rayleigh waves. Bull. Seismol. Soc. Am. 101, 2162–2175.

Denolle, M. A., E. M. Dunham, G. A. Prieto, and G. C. Beroza (2014), Strong ground motion prediction using virtual earthquakes, Science, 343, 399–403, doi:10.1126/science.1245678.

Denolle, M. A., H. Miyake, S. Nakagawa, N. Hirata, and G. C. Beroza (2014), Long-period seismic amplification in the Kanto Basin from the ambient seismic field, Geophys. Res. Lett., 41, doi:10.1002/2014GL059425.

Frankel, A. D., W. J. Stephenson, and D. L. Carver, 2009. Sedimentary basin effects in Seattle, Washington: Ground-motion observations and 3D simulations. Bull. Seism. Soc. Am. 99, 1,579–1,611

Liu, P-C., and R. J. Archuleta (2002). The effect of a low-velocity surface layer on simulated ground motion, Seism. Res. Lett. 73, 267.

Lobkis, O. I., and R. L. Weaver (2001), On the emergence of the Green's function in the correlations of a diffuse field, J. Acoust. Soc. of Am., 110, 3001–3017, doi:10.1121/1.1417528.

Prieto, G. A., and G. C. Beroza (2008), Earthquake ground motion prediction using the ambient seismic field, Geophys. Res. Lett., 35, L14304, doi:10.1029/2008GL034428.

Prieto, G. A., M. Denolle, J. F. Lawrence, and G. C. Beroza (2011), On amplitude information carried by the ambient seismic field, C. R. Geosci., 343, 600–614.

Shapiro, N. M., M. Campillo, L. Stehly, and M. H. Ritzwoller (2005), High-resolution surface wave tomography from ambient seismic noise, Science, 307, 1615–1617, doi:10.1126/science.1108339.

Stehly, L., Campillo, M. & Shapiro, N.M., 2006. A study of the seismic noise from its long-range correlation properties, J. geophys. Res., 111, 1–12.

Stephenson, W. J. (2007). Velocity and density models incorporating the Cascadia Subduction Zone for 3D earthquake ground motion simulation, U.S. Geol. Surv. Open-File Rept. OF 2007-1348, 24 pp.

Tian, Y., and M. H. Ritzwoller (2015), Directionality of ambient noise on the Juan de Fuca plate: implications for source locations of the primary and secondary microseisms, Geophys J Int, 201(1), 429–443, doi:10.1093/gji/ggv024.

Toro, G. R., N. A. Abrahamson, and J. F. Schneider (1997), Model of strong ground motion from earthquakes in Central and Eastern North America: Best estimates and uncertainties, Seismol. Res. Lett., 68, 41–57, doi:10.1785/gssrl.68.1.41.

Tsai, V. C. (2011), Understanding the amplitudes of noise correlation measurements, J. Geophys. Res., 116, B09311, doi:10.1029/2011JB008483.

Wang, P.-L., S. E. Engelhart, K. Wang, A. D. Hawkes, B. P. Horton, A. R. Nelson, and R. C. Witter (2013), Heterogeneous rupture in the great Cascadia earthquake of 1700 inferred from coastal subsidence estimates, J. Geophys. Res. Solid Earth, 118, doi:10.1002/jgrb.50101.

CHAPTER 4. SUMMARY AND FUTURE WORK

4.1 CONCLUSIONS

We briefly summarize the key results from the studies in this thesis.

We find correlation between tremor (slow slip) and slab earthquakes at Nankai subduction zone. Tremor and inferred slow slip are triggered by slab earthquakes, but not vice versa. The physical mechanism for the triggering of tremor is likely to be the dynamic stress of S wave from slab earthquakes.

The deep long-period earthquakes beneath Mount St. Helens show sensitivity to the solid Earth tides. Compressional tidal stress appears to elevate the DLP activity. In the investigated time window, DLPs do not show significant correlation with subduction zone ETS and shallow seismicity. The source of DLPs from the productive source region may vary, since diverse S wave polarization are observed.

We use ambient noise correlation to retrieve the empirical green's functions. The amplitude measured from noise EGFs are generally consistent with those measured from teleseismic S wave and numerical simulations, which suggests noise EGFs contain useful amplitude information that can be interpreted by geometrical spreading, attenuation, amplification. The ground motion is amplified by a factor of up to 3 when wave propagating in west-east direction. Both the uncertainties of EGFs and synthetic waveforms need further investigation, especially with seismic data and scenario events from wide azimuthal range.

4.2 FUTURE WORK

Several of these studies can be continued to extend the results.

We have shown in chapter 1 that the tremor (slow slip) can be triggered by the dynamic stress of high frequency waves from nearby small earthquakes. Previous studies have also shown that the tremor can be modulated by tidal stress, transient stress associated with surface waves of large distant earthquakes, and static stress change of earthquakes. These driving stresses have various loading frequencies. One interesting question is what is the role for stress amplitude and loading frequency in modulating tremor activity? To answer this question, a more comprehensively observational study is required to quantify triggering rate of tremor with comparable measurement for these driving forces. In addition, physical experiments and numerical simulations with physically reasonable conditions (parameters) and various loading stress might also be needed to investigate the physical regime of the faulting system during tremor (slow slip) evolution.

We have not inverted for the focal mechanism for the DLPs beneath Mount St. Helens. We discussed the challenging nature of focal mechanism inversion for DLPs in chapter 2. In the future, a close monitoring of DLP activity and shallow seismicity with dense instruments is still required. A new and high-resolution seismic velocity model is coming from the iMUSH project. Such model would help reduce the complications from unknown structure in inverting for the source parameters of DLPs.

We only exploit ambient seismic data from the Puget Sound linear array. All observations should only represent measurements in west-east direction. Ground motion amplification may show different patterns with incoming source from north or south. Therefore, seismic data from a 2D array is desired to investigate the direction dependency of amplification based on noise correlation. The time period is short (from February to April), so the results could be biased from nonstationary characteristics of the ambient noise field due to seasonal variation. Using a longer time window may reduce such bias. The bias of EGFs due to noise energy directivity needs to be

better quantified, especially when dealing with 2D data. We only compare the EGFs from noise correlation with synthetics from moment tensor source. One natural extension would be comparing the EGFs with synthetics from a point-force source and seismograms from real earthquakes, such that we can systematically quantify the uncertainty of the EGFs and current velocity model used in numerical simulations.